DETONATION PERFORMANCE ANALYSIS OF COCRYSTAL AND OTHER

MULTICOMPONENT EXPLOSIVES

A Dissertation

Submitted to the Faculty

of

Purdue University

by

Vasant S. Vuppuluri

In Partial Fulfillment of the

Requirements for the Degree

of

Doctor of Philosophy

May 2019

Purdue University

West Lafayette, Indiana

THE PURDUE UNIVERSITY GRADUATE SCHOOL
STATEMENT OF DISSERTATION APPROVAL

Dr. Steven F. Son, Co-Chair
>School of Mechanical Engineering

Dr. I. Emre Gunduz, Co-Chair
>Naval Postgraduate School

Dr. Christopher S. Goldenstein
>School of Mechanical Engineering

Dr. Davin G. Piercey
>School of Mechanical Engineering, School of Materials Engineering

Approved by:
>Dr. Jay Gore
>>Head of the Graduate Program

ACKNOWLEDGMENTS

It has been the privilege of a lifetime to have interacted with the people of Maurice J. Zucrow Laboratories. First and foremost, I would like to thank Prof. Steve Son and Prof. I. Emre Gunduz for having given me the opportunity to pursue this degree at Purdue. Words cannot do justice to the value of the time I spent at Purdue. In addition, I am deeply grateful to Prof. Steve Son and Prof. Emre Gunduz for their patience and support throughout my time at Purdue. I would also like to thank Prof. Davin Piercey and Prof. Chris Goldenstein for serving on my committee. This work was supported through US Army Research Office Contract No. W911NF-13-1-0387.

To quote the words of students before my time and also Isaac Newton, this work has stood on the shoulders of giants. This work would not have been possible without the help of Dr. Jonathan C. Bennion (formerly University of Michigan, now Army Research Laboratory), Ren C. Wiscons (University of Michigan), and Rosayln V. Kent. Jon and Ren made the trip from Ann Arbor to West Lafayette twice for synthesis of the CL-20/HP solvate. I would also like to thank Jon for teaching me how to make the CL-20/HP solvate. Rosalyn and Ren spent countless hours on synthesis of ADNP and ADNP/DAF cocrystal. Phil Samuels was kind enough to supply me with CL-20 and cocrystals when needed at great cost to the government.

I would also like to thank Nick Cummock in particular for his help in teaching me microwave interferometry, which is the bedrock of this work. I am extremely grateful for his patience and willingness to help me learn this technique. Additionally, I would like to thank Nick Cummock and Gabriel Montoya for their help with using the streak camera. When I was busy with teaching ME 200 as a Lambert Fellow in the Fall 2018 semester, Gabe and Nick spent countless hours troubleshooting the streak camera to

get it ready for me to use. Finally, I would like to thank my family for having been there for me my entire life. I would not have made it to this point without the love and support of my parents and brother.

TABLE OF CONTENTS

LIST OF TABLES

LIST OF FIGURES

ABBREVIATIONS

HMX	cyclotetramethylene tetranitramine
RDX	cyclotrimethylene trinitramine
CL-20	hexanitrohexaazaisowurtzitane
TNT	trinitrotoluene
TATB	triaminotrinitrobenzene
ADNP	4-amino-3,5-dinitropyrazole
DAF	3,4-diaminofurazan
PETN	pentaerithrytol tetranitrate
DNBT	5,5-Dinitro-2H,2H-3,3-bi-1,2,4-triazole
DNP	dinitropyrazole
AP	ammonium perchlorate
MDNT	1-methyl-3,5-dinitro-1,2,4-triazole
HP	hydrogen peroxide
PBX	polymer-bonded explosive
C-J	Chapman-Jouguet
TMD	theoretical maximum density
IHE	insensitive high explosive
IM	insensitive munition
STFT	Short Time Fourier Transform
FFT	Fast Fourier Transform
CWT	continuous wavelet transform
R-H	Rankine-Hugoniot
ESD	electro-static discharge
DDT	deflagration-to-detonation transition

ABSTRACT

Vuppuluri, Vasant S. Ph.D., Purdue University, May 2019. Detonation Performance Analysis of Cocrystal and Other Multicomponent Explosives. Major Professor: Steven F. Son and I. Emre Gunduz, School of Mechanical Engineering.

Development of novel energetic molecules is a challenging endeavor. Successful discovery and synthesis of a novel viable energetic molecule is an even more challenging endeavor. To qualify for scale-up in production, the molecule must undergo extensive characterization at the small scale and meet criteria for sensitivity, stability, toxicity, lifetime, etc. A failure to qualify for further scale-up can result in significant wasted investment. Cocrystallization of energetic materials is a potentially attractive route to development of new energetic materials because existing molecules can be used to create new materials that have tailored properties different from either coformer. A cocrystal is a combination of two crystalline monomolecular materials that yields a material with a unique crystal structure. While cocrystallization reduces the front-end investment ordinarily required for discovery of new energetic molecules, discovery of energetic cocrystals is not trivial. A number of energetic cocrystals have been reported that display attractive properties such as high density and improved thermal stability. However, the effect of cocrystal formation on larger scale properties, particuarly detonation properties, is not well-understood. Knowledge of these properties is important for understanding the potential improvements gained from pursuing discovery of cocrystals.

A challenge with obtaining detonation properties is that most techniques typically require anywhere from hundreds of grams to several kilograms of material. For example, rate stick experiments typically have an L/D (length to diameter) ratio between 12 and 20. Even for ideal explosives, diameters used are typically at least two cen-

timers in diameter. Such experimental configurations are poorly suited for materials in the early stages of development.

In this work, comparative detonation velocity measurements were performed for select hexanitrohexaazaisowurtzitane (CL-20) cocrystals that have been reported in the past five years along with corresponding formulations or physical mixtures of the components. The detonation velocity measurements were performed using microwave interferometry, a well-established detonation velocity diagnostic. Using precision-machined hardware and appropriate matching of booster charge to sample charge, it was shown with statistical analysis that well-resolved measurements of detonation velocity could be obtained with shot-to-shot variation in the range of 130 m/s. The detonation velocity for cyclotetramethylene tetranitramine (HMX) was obtained using this experimental technique to validate the method and estimated variation. It was demonstrated that detonation tests with good repeatability could be performed for the nearly ideal explosives considered.

The experimental technique described above was performed first for a cocrystal of 1-methyl-3,5-dinitro-1,2,4-triazole (MDNT) and CL-20. Comparative measurements were performed for the cocrystal and physical mixture at a loading density of 1.4 g/cm^3. We chose a fixed loading density in order to isolate isolate effects other than loading density. The cocrystal was observed to detonate about 500 m/s faster than the physical mixture. In comparison, thermochemical equilibrium predictions showed that the cocrystal would detonate about 230 m/s faster than the physical mixture at this density. The enthalpy of formation for this cocrystal was double that of the physical mixture and this difference resulted in the predicted difference. Similar measurements were performed for the cocrystal of cyclotetramethylene tetranitramine (HMX) and CL-20 and CL-20/hydrogen peroxide (HP) solvate at the same loading density. The HMX/CL-20 cocrystal was observed to detonate about 300 m/s faster than the physical mixture. The CL-20/HP solvate was observed to detonate about

300 m/s faster than CL-20.

Using the Kamlet scaling laws, it was determined that the differences in detonation velocity observed are attributable to differences in enthalpy of formation. That is, the energy state is different between the configurations. The enthalpy of formation for MDNT/CL-20 was measurably larger than its physical mixture. The CL-20/HP solvate was also measurable larger than that of CL-20. This result has implications for intermolecular bond and configurational energies formed in cocrystals that affects their energy content. Fully explaining the precise reason for this, and perhaps exploiting this in future cocrystals and multimolecular systems is a challenge for modelers, theoreticians, and synthesis chemists.

1. INTRODUCTION

1.1 Motivation

There is a constant demand for new energetic materials tailored for specific applications. For example, in explosive boosters for nuclear weapons, insensitivity is at least as important as high performance. However, the process of qualifying a new energetic material for use in any type of application is lengthy, taking decades or more.

The conventional route to developing a new energetic material is discovery and initial synthesis of a novel energetic molecule in small quantities. Extensive characterization of sensitivity and thermal stability at small scale is then performed on the new energetic molecule. A thorough understanding of the thermal stability and sensitivity (e.g. impact, electro-static discharge (ESD), friction, etc.) of the new energetic molecule is needed before scaling up production further. A molecule may fail to qualify for further synthesis for a number of reasons, including unacceptable results obtained from small-scale characterization or other reasons such as cost or toxicity.

Explosive materials are typically pressed or otherwise molded into various geometries. In order to facilitate this, energetic molecules are commonly used in explosive formulations known as polymer-bonded explosives (PBXs), which consist of the crystalline explosive, the binder, and various other additives. For example, PBX 9502 is an insensitive high explosive (IHE) formulation consisting of 95% 1,3,5-triamino-2,4,6-trinitrobenzene (TATB) and 5% fluoropolymer binder which can be pressed to high density and machined to desired shapes [1]. However, extensive study of compatibility of the molecule with the binder material or other ingredients is needed before large-scale development of new PBX materials or similar formulations can be

commenced.

The performance characteristics of candidate energetic materials must also be investigated. Detonation velocity and pressure are two of the most important performance parameters for explosives but there are a number of other aspects of detonation performance such as critical diameter and corner turning. Detonation performance experiments however require anywhere from several hundreds to thousands of grams of material, an amount that often exceeds the supply of energetic materials in the developmental stage.

The first major challenge to developing new explosives is associated with discovery of a candidate molecule that successfully qualifies for scale-up in production after small-scale testing. By this time, a number of molecules in the discovery phase will have failed to be viable energetic molecules. Those that are found to be viable will have then failed to qualify based on small-scale characterization. Another major challenge is in performing detonation experiments due to the expense of scaling up materials in the developmental stage and the cost of large-scale detonation experiments.

For this reason, formation of cocrystals has been explored as a possible route to development of new energetic materials. A cocrystal is a combination of two or more mono-molecular materials that results in a new multi-molecular material with a unique crystal structure. A potential advantage of this route to energetic material development is that it may reduce the front-end investment that is typically required for successful discovery and synthesis of a novel energetic molecule. Instead, existing mono-molecular crystalline materials can be used to obtain a new multi-molecular material with potentially favorable properties. A number of energetic complexes have been reported that show favorable properties such as high density. However, comparatively less work has been done to investigate detonation properties of these materials. There is also comparatively less work done to understand the effect of

cocrystallization on detonation properties. Detonation experiments are challenging owing to the need for large amounts of material for conventional tests. Therefore, precision small-scale testing is useful.

While the use of existing energetic molecules reduces the front-end investment ordinarily required, discovery of energetic cocrystals is not trivial. Therefore, an important question relating to energetic cocrystals is how the cocrystal is different from a physical mixture or formulation of the components. It has been shown that small-scale properties of cocrystals such as density are noticeably altered compared to a physical mixture of the components. The energy state can also change as a result of cocrystallization. However, integrated properties, particularly detonation properties, are not well-explored. This understanding is crucial to deciding appropriate directions for cocrystals as new energetic materials.

1.2 Cocrystals

1.2.1 Overview

The study of cocrystals is a facet of the broad discipline of crystal engineering, which is the modification of properties at the crystalline level for a desired application. The hierarchy of material properties begins at the molecular level. In the context of energetic materials, properties that emerge at the molecular level include detonability and oxygen balance among others. For example, the presence of nitro groups in energetic molecules such as HMX gives rise to its detonability [2]. The oxygen balance is a major determinant of the products that form [1]. The next level above the molecular organization is the crystalline level.
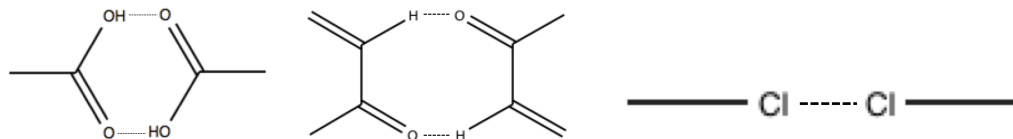
Figure 1.1. Examples of intermolecular interactions: $OH \cdots O$ (left), $CH \cdots O$ (center), halogen bond (right) (used with permission) [3].

Crystals form by means of intermolecular interactions of functional groups [3]. These interactions are known as supramolecular synthons. Hydrogen bonding is a major intermolecular interaction that influences crystal formation [3]. It is the most ubiquitous intermolecular interaction seen in crystal formation due to the large number of functional groups that interact based on hydrogen bonding. Intermolecular interactions of the form AHB have been observed such that hydrogen, denoted by H is covalently bonded to molecule A, which is more electronegative than hydrogen [4]. The interaction between the H and molecule B is known as a hydrogen bond [4, 5]. Another important intermolecular interaction is halogen bonding, in which atoms of halogens in close proximity to each other form short, nonbonded contacts [3]. Examples of these intermolecular interactions are shown in Fig. 1.1. This bonding and configurational energy can change the energy contained within a crystalline explosive.

The principles that govern the emergence of crystal structure are applicable to cocrystals. Cocrystals are a subset of complexes, which are binary molecular systems that interact to form an ordered crystal structure [6]. Using this hierarchy, solvates and hydrates are also subsets of complexes. Solvates are complexes where one of the components is a liquid at standard temperature and pressure. A hydrate is a binary system wherein one of the components is water.

Similar to development of novel energetic materials, development of novel pharmaceutical compositions is challenging. Cocrystallization has therefore been of particular interest in the pharmaceutical industry. Pharmaceutical compositions typically con-

sist of the active pharmaceutical ingredient (API) and other components such as binders [7]. The solubility of an API depends upon crystal structure and is a critical element of bioavailability, which is critical to the efficacy of treatment using a particular drug [8]. Polymorphism is the phenomenon by which a monomolecular material may have multiple crystal structures and many energetic materials such as 1,3,5,7-Tetranitro-1,3,5,7-tetrazocane (HMX) exhibit this phenomenenon [9]. Polymorphism is also common with crystalline APIs and it has an observable effect on their solubility [8, 10]. Cocrystallization has therefore been of interest for pharmaceuticals because it offers an additional route to tuning relevant properties such as solubility [8].

1.2.2   Energetic Cocrystals

The guidance for the formation of energetic complexes comes in part from work that has been done on pharmaceutical complexes. In the context of energetic materials, the properties that are of the most interest include density, sensitivity, and detonation performance among other properties. It is well known that density of an energetic material is a significant determinant of detonation performance [1, 11]. Of the supramolecular synthons that contribute to complex formation, only a small subset are available to form energetic cocrystals. In energetic materials that are in widespread use today, the most common functional groups are nitro, methyl, and amino groups [1]. While this has posed a challenge to forming viable energetic complexes, a number of these materials have been reported.

Studies in recrystallization of explosives have yielded discovery of solvates. Similar to cocrystals, solvates may have prove to have favorable properties. For example, it has long been known that HMX forms a solvate with N,N-dimethylformamide (DMF) and

was found to exhibit reduced impact sensitivity compared to that of pure HMX [12]. Using single-crystal X-ray diffraction (SCXRD), Cobbledick *et al.* measured the density of this solvate to be 1.612 g/cm^3 [13]. While the HMX/DMF solvate exhibits lower impact sensitivity than that of pure HMX, its reduced density results in a reduction in detonation performance. Despite this, the HMX/DMF solvate is among the earliest examples of an energetic material forming a complex exhibiting novel properties.

Landenberger *et al.* reported the formation of a number of complexes of trinitrotoluene (TNT) with various inert compounds such as naphthalene [14]. It was found from this study that a cocrystal of TNT and 1-bromonapthalene yielded a cocrystal that was denser than either of the components [14]. While bromonaphthalene is not known to be detonable, the ability to yield a cocrystal whose density exceeds the components is an important finding since density affects detonation properties. Landenberger *et al.* also reported the synthesis of a number of HMX complexes. The authors identified conformations for HMX within these complexes as well as densities and impact sensitivities of the complexes [15]. In contrast to the TNT complexes reported previously, no HMX complex had a density that exceeded that of HMX. Similar to the TNT complexes reported however, all of the HMX complexes reported by Landenberger *et al.* exhibited reduced impact sensitivity compared to that of HMX [15].

Bolton *et al.* reported the successful synthesis of the first energetic-energetic cocrystal of TNT and hexanitrohexaazaisowurtzitane (CL-20) in a 1:1 molar in 2011. The molecular structure of TNT and CL-20 are shown in Figs. 1.2 to 1.3. TNT is a well-known, relatively insensitive energetic material that exhibits the useful property of having a stable melt phase [1]. However, it exhibits relatively poor detonation performance due to poor oxygen balance (-74%) and its low density (1.65 g/cm^3) among other factors [1]. However, it has a stable melt phase, making it useful in

melt-castable compositions such as Octol and Composition B in which it functions as an energetic binder [1]. CL-20 is currently the most powerful commercial explosive primarily due to its high density [16]. The compound was first synthesized in 1986 at Naval Air Warfare Center Weapons Division (NAWCD), China Lake, CA [17]. CL-20 exists in the four stable polymorphs (or conformations) of β, γ, α, and ϵ CL-20. The α polymorph is typically a CL-20 hydrate with water molecules in voids. The most stable, dense polymorph of CL-20 is the ϵ form with a density of 2.044 g/cm^3 [17]. The ϵ polymorph is also the least sensitive polymorph of CL-20. However, one of the steps in the CL-20 synthesis procedure involves the use of a palladium-on-carbon catalysis reaction [17]. In addition, while the ϵ polymorph is the most thermodynamically favored form of CL-20 at standard temperature and pressure, the β polymorph can also exist at room temperature. The α hydrate may also precipitate. It is therefore difficult to obtain high phase purity of the ϵ polymorph due to concomitant growth of other CL-20 polymorphs in most crystallization methods [18]. For these reasons, the cost of CL-20 is high and this has precluded wider adoption in energetics applications.
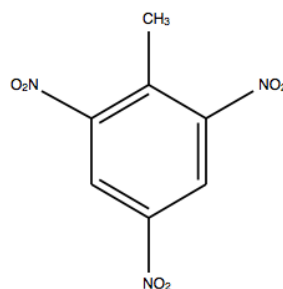
Figure 1.2. TNT molecular structure.

The TNT/CL-20 cocrystal was found to exhibit lower impact sensitivity than that of $\epsilon-$CL-20. In addition, this cocrystal was formed using the CH $\cdots$ O synthon, demonstrating the potential for energetic cocrystal formation using other coformers given the abundance of this interaction in energetic materials [19]. It was shown with
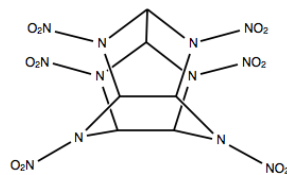
Figure 1.3. CL-20 molecular structure.
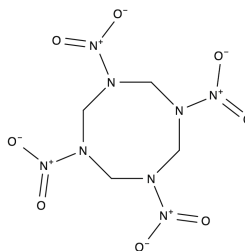
Figure 1.4. HMX molecular structure.

various TNT and HMX complexes that it was possible to separate the components by holding them at slightly elevated temperature [14,15]. Bolton *et al.* extended this concept to the TNT/CL-20 cocrystal and showed that after heating the cocrystal to 136 °C and holding at this temperature, the cocrystal separated into liquid TNT and $\gamma-$CL-20. This effect could be exploited as a way to change sensitivity of the material by heating [19]. In addition, the density of this cocrystal was measured to be 1.84 g/cm^3, which is comparable to that of PBX 9501 [19]. This result demonstrated that the cocrystal has good potential as an explosive, especially if a less expensive synthesis method for CL-20 could be developed.

In 2012, Bolton *et al.* reported another energetic-energetic cocrystal with CL-20 as a coformer-the HMX/CL-20 cocrystal in a 1:2 molar ratio [20]. The layered structure of HMX/CL-20 is shown in Fig. 1.5 with the HMX molecules shown in blue and the CL-20 molecules shown in yellow [20]. Similar to the TNT/CL-20 cocrystal, the HMX/CL-20 cocrystal was also found to exhibit reduced impact sensitivity compared to that of $\epsilon-$CL-20, with a value comparable to that of $\beta-$HMX, the most stable
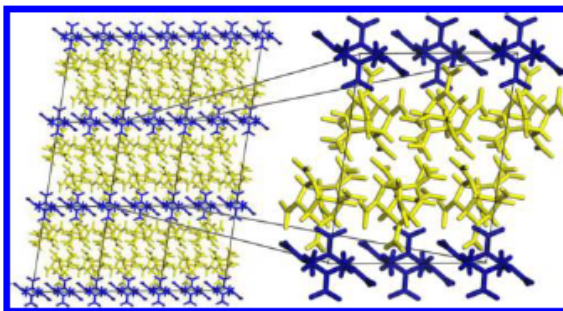
Figure 1.5. Layered structure of HMX/CL-20 cocrystal [20].

and least sensitive polymorph of HMX [20]. Using single-crystal X-ray diffraction (SCXRD), the density of this cocrystal was measured to be 1.945 g/cm^3, making it denser than any polymorph of HMX [20].

HMX/CL-20 and TNT/CL-20 are both the oldest energetic-energetic cocrystals. Additional researchers have reported the synthesis of the TNT/CL-20 cocrystal. Yang *et al.* prepared the TNT/CL-20 cocrystal using a solvent/anti-solvent method [21]. The sensitivity results affirmed those of Bolton *et al.* [19, 21]. A significant question with cocrystals is how the properties of a cocrystal differ from those of a physical mixture. It has been shown that the density of the HMX/CL-20 and TNT/CL-20 cocrystal is different from the respective physical mixtures. Accordingly, Yang *et al.* showed that the cocrystal was less sensitive than a physical mixture of the components. Additionally, it is important to understand how the detonation properties of a cocrystal are different from those of a physical mixture. Yang *et al.* measured the detonation velocity of the TNT/CL-20 cocrystal and physical mixture. The difference in the loading density between the cocrystal and physical mixture test samples was 3.5% [21]. The cocrystal was observed to detonate about 400 m/s faster than the physical mixture, which is a difference of about 4.6% [21]. Yang *et al.* concluded that a higher pressing density was achievable with the cocrystal compared to the physical mixture pressed to the same pressure, which resulted in a higher measured detonation velocity for the cocrystal [21]. Aldoshin *et al.* also studied the TNT/CL-20 cocrystal.

In contrast to Bolton *et al.*, Aldhosin *et al.* claimed that the primary interactions driving this cocrystal were van der Waals forces between nitrogen bonds [22]. The authors also studied the thermal behavior of the TNT/CL-20 cocrystal and observed only a single exotherm in contrast to Bolton *et al.*, although this difference may be attributable to differing experimental conditions, including the type of purge gas used and whether the pans were sealed or open during temperature ramp-up [19, 22].

Since the discovery of the first two energetic-energetic cocrystals of CL-20, CL-20 has been a major focus of cocrystal discovery efforts. In 2015, Goncharov *et al.* reported the successful synthesis of bimolecular cocrystals of 2,4-dinitro-2,4-diazapentane (DNP) and 2,4-dinitro-2,4-diazaheptane (DNG) [23]. The CL-20/DNP cocrystal had a crystal density of 1.928 g/cm^3, which is higher than that of HMX and comparable to the density of the HMX/CL-20 cocrystal. [1, 20]. The measured velocity of this cocrystal at a loading density of 98% TMD was measured to be 9 km/s [23]. For comparison, the detonation velocity of HMX at the same loading density is measured to be 9.11 km/s [24]. Another cocrystal reported in 2015 was a cocrystal of 1-methyl-3-5-dinitro-1,2,4-triazole (MDNT) and CL-20 in 1:1 molar ratio. MDNT is an energetic heterocyclic azole-based compound whose structure is shown in Fig. 1.6 [25] The azole class of energetics has been of interest in research into melt-castable energetics in order to replace TNT in melt-castable explosive formulations [26]. In 2015, Anderson *et al.* reported the formation of a cocrystal of MDNT and CL-20 in a 1:1 molar ratio. A noteworthy feature of this cocrystal was the nature of the intermolecular interactions driving cocrystal formation. In the TNT/CL-20 and HMX/CL-20 cocrystals, CH$\cdots$O hydrogen bonding between methyl and nitro groups was largely what drove cocrystal formation. In contrast to these two cocrystals, the formation of the MDNT/CL-20 cocrystal was largely driven by electrostatic interactions between the nitro groups in CL-20 and the triazole ring of MDNT [27]. The density of the cocrystal was measured to be 1.883 g/cm^3 [27].
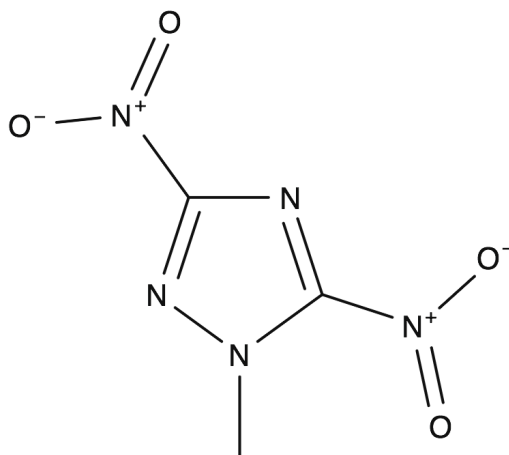
Figure 1.6. MDNT Structure.

The formation of hydrates and solvates is generally viewed an undesirable effect with energetic materials. For example, George *et al.* reported a number of solvates of HMX that were all of lower density than any polymorph of HMX [12]. In addition, Millar *et al.* reported the formation of a number of CL-20 solvates with solvent coformers such as DMF and butyrolactone. All of these solvates were of lower density than all known polymorphs of CL-20 [28]. Due to reduced density, there is likely to be a reduction in the detonation velocity and pressure of these solvates. In 2016, Bennion *et al.* reported the formation of two hydrogen peroxide (HP) solvates of CL-20. One of these solvates, known as the orthorhombic solvate, was found to have a crystal structure that is nearly indistinguishable from that of α-CL-20 and its density was 2.033 g/cm^3, close to the density of ϵ-CL-20. The α hydrate of CL-20 has a density of 1.97 g/cm^3, making the orthorhombic solvate denser than the α-CL-20 hydrate [29]. The monoclinic form was slightly lower in density than the α-CL-20 hydrate but the presence of hydrogen peroxide results in greater energetic content.

Similar to CL-20, 5,5'-dinitro-2H,2H'-bi-1,2,4-triazole (DNBT) has a drawback of high propensity to form hydrates [30]. DNBT is a high-nitrogen energetic material

first identified in the 1970s [31]. Dippold *et al.* measured its density to be 1.90 g/cm^3, which is comparable to that of HMX [32]. Wiscons *et al.* demonstrated the formation of two hydrogen peroxide solvates of DNBT, both of which were denser than the DNBT monohydrate [33]. The formation of hydrogen peroxide solvates in this manner is a possibly less expensive alternative to obtaining DNBT in a form that will provide good energetic performance.

While the conformational diversity of CL-20 has been a major factor in why it has been the major focus of cocrystalliation studies, cocrystals based on energetic heterocycle compounds have also been studied . In 2015, Bennion *et al.* reported the synthesis of a cocrystal of 1,3-dinitropyrazole (DNP) and DNBT in a 2:1 molar ratio. DNP is another energetic heterocycle [34]. DNP was found to have comparable impact sensitivity to that of ϵ-CL-20 while the DNBT/DNP cocrystal was found to have an impact sensitivity close to that of DNBT. However, the density of the cocrystal was 1.871 g/cm^3, which is comparable to that of DNBT [30]. To the knowledge of the author of this work, the detonation velocity of neither DNBT, DNP, nor the cocrystal has been reported. Despite this, the high density of the cocrystal implies good potential as an explosive. In all cases of energetic-energetic cocrystals discussed herein, the densities of the cocrystals have ended up in between those of the component materials. With CL-20 cocrystals discussed so far, this has resulted in a noticeable reduction in density, implying degradation of detonation velocity and pressure compared to that of ϵ-Cl-20. In the case of the DNBT/DNP, the density of the cocrystal was comparable to that of DNBT, the high-density component, which demonstrated possible synergistic interaction of the components. The density of a cocrystal is dependent on the available intermolecular interactions that determine the packing arrangement of the component materials.

Another noteworthy cocrystal involving energetic heterocycle compounds is the ADNP/DAF cocrystal. 4-amino-3,5-dinitropyrazole (ADNP) (also known as LLM-116)

is a relatively insensitive explosive whose synthesis was first reported in 2001 [35]. In small-scale sensitivity testing, ADNP was found to have impact and friction sensitivity comparable to that of TATB [36]. The detonation velocity of LLM-116 was measured to be 8.13 km/s, which is comparable to that of PBX 9502, a TATB-based IHE formulation [36, 37]. However, a drawback of ADNP is its poor thermal stability [36]. 3,4-diaminofurazan (DAF) is an energetic precursor to compounds such as 3,3'-diamino-4,4'-azoxyfurazan (DAAF) [38]. Bennion *et al.* reported the formation of a cocrystal of ADNP and DAF exhibiting improved thermal stability compared to that of ADNP [39]. The cocrystal was also observed to have a stable melt phase. In contrast to the irreversible separation of the TNT/CL-20 cocrystal upon heating, the ADNP/DAF cocrystal was found to revert to the cocrystal form upon cooling to room temperature from the melt temperature of approximately 160 °C. No other cocrystal reported thus far has been reported to modify thermal stability in this manner. Such behavior enables large-scale production through melt recrystallization.

1.2.3 Cocrystal Production Methods

The production of cocrystals often involves the use of standard techniques for crystallization. The conventional method for preparation of cocrystals involves dissolving the components in a suitable solvent such that the cocrystal form precipitates out of solution. This process is referred to as slow evaporation. If the cocrystal is more thermodynamically favored than the individual components, the cocrystal will precipitate out of solution. This depends not only on the relative thermodynamic stability of the cocrystal form but also the choice of solvent. The key requirement of a cocrystal is that the component molecules must interact to form an ordered structure. A number of characterization techniques are used to prove the formation of a cocrystal. The most reliable method to prove the formation of a cocrystal is SCXRD [40]. Practitioners also commonly use infrared (IR) and Raman spectroscopies to offer additional evidence of cocrystal formation [40]. While single crystals grown from slow

evaporation can provide conclusive evidence of cocrystal formation, this method is likely unsuitable for large-scale production. Therefore, production methods suited for large-scale production is another important focus of research into cocrystals. As is the case with cocrystal discovery, the guidance for large-scale production methods comes from studies involving pharmaceutical cocrystals.

Etter *et al.* demonstrated formation of a number of nitroaniline cocrystals using solid-state grinding [41, 42]. Friscic *et al.* conjectured that in solid-state grinding, the intermolecular bonds in the component materials are broken due the forces of grinding, resulting in formation of intermolecular bonds between the components resulting cocrystal formation [43]. This method though may not be suitable for energetic cocrystals due to their potential to react during the grinding process.

Resonant mixing is another production method for cocrystal production. In resonant mixing, a base-plate is operated at resonance to maximize energy transfer to the mixing medium [44]. In 2014, am Ende *et al.* used resonant mixing to produce a cocrystal of carbamazepine and nicotinamide (CBZ/NCT). Using this method, the authors were able to produce 22 g of CBZ/NCT cocrystal in one hour [45]. This result showed the promise of the method of resonant mixing as a large-scale production technique. The authors applied this technique to produce 40 g of the HMX/CL-20 cocrystal in one hour [46]. The MDNT/CL-20 cocrystal was also scaled up with this method [47]. Hope *et al.* studied temperature rise during the process and found that the bulk temperature is in the range of 45-50 °C, indicating that bulk temperature rise may be within safe operating parameters for many energetic materials [48]. It should be noted that while the bulk temperature rise was relatively modest, localized heating due to friction can be extensive and morphologies of the particles may result in reaction due to hotspots so appropriate care should be taken. Also, the authors noted that large piles can trap thermal energy. In another study in 2015, Qiu *et al.* demonstrated the use of aqueous suspension ball milling. In ball milling, grinding

media are used to break up large particles. To mitigate the potential of friction-induced reaction, Qiu *et al.* suspended the CL-20 and HMX in a mixture of water and polyvinyl alcohol. Full conversion to the cocrystal form was achieved in one hour with nanometer sized particles formed in the process [49]. The aforementioned strategies of cocrystal production all involve the use of solvents and agitation to disrupt the equilibrium such that the cocrystal conversion will occur once equilibrium is regained.

Medina *et al.* demonstrated the use of a solvent-free technique known as twin-screw extrusion as a large-scale production [50]. Boksa *et al.* demonstrated the use of a technique known as matrix-assisted grinding (MAG) in which the coformers embedded in binder matrix are continuously converted to cocrystal once the binder is heated to its melting temperaure [51]. Both these techniques demonstrate potentially attractive methods for large-scale production of cocrystals and also PBXs containing these explosives.

1.2.4 Summary

A number of energetic cocrystal systems are being studied. A unifying theme of these studies has been to identify and leverage synergistic interactions of molecules to form cocrystals that overcome weaknesses of the component molecules. The majority of the cocrystal systems studied this far have been focused on overcoming drawbacks associated with sensitivity of the component materials. Many cocrystals have been reported that have high density which is indicative of their potential as high-performing explosives. However, there remains significant characterization to be done.

1.3 Microwave Interferometry

1.3.1 General Principles

Microwave interferometry (MI) is a well-known technique for measuring detonation velocity and transient events such as shock-to-detonation transition. In using MI to track surface motion, a microwave signal is transmitted to the reflective surface. The signal reflected from the moving surface interferes with the incident or reference signal to produce a fringe pattern. The basis of microwave interferometry is the dielectric permittivity of materials, which relates to their propensity to experience polarization due to electromagnetic radiation. The dielectric permittivity is commonly normalized to the vacuum permittivity as:

$$\epsilon_r = \frac{\epsilon}{\epsilon_0}, \tag{1.1}$$

where ϵ_r is the relative permittivity and ϵ_0 is the permittivity of the free space or vacuum [52]. In this work, the permittivity will always refer to the relative permittivity. The permittivity split into real and imaginary components is

$$\epsilon_r = \epsilon_r^{'} - j\epsilon_r^{''}, \tag{1.2}$$

where $\epsilon_r^{'}$ and $\epsilon_r^{''}$ are respectively real and imaginary components of permittivity and $j = \sqrt{-1}$ [52]. The imaginary component quantifies the absorption of electromagnetic radiation [53]. The dielectric loss coefficient is defined as [52]

$$\tan\delta = \frac{\epsilon_r^{''}}{\epsilon_r^{'}}. \tag{1.3}$$

Most energetic materials have a loss coefficient of 0.01 or less, which makes them nearly transparent to microwaves [54]. The permittivity of a mixture can be calculated according to the Landau-Lifshitz/Looyenga relation given as

$$\epsilon_r^{1/3} = \left(\epsilon_{r,A}^{1/3} - \epsilon_B^{1/3}\right) V_A + \epsilon_{r,B}^{1/3}, \tag{1.4}$$

where $\epsilon_{r,A}^{1/3}$ and $\epsilon_B^{1/3}$ are the respective permittivities of components A and B and V_A is the volume fraction occupied by air [55]. Other mixture relations may be used

to determine dielectric constants for porous materials [56]. Eq. (1.4) can be recast to represent the permittivity of a granular material as a function of bulk or powder density. This relation is

$$\epsilon_r^{1/3} = \left(\epsilon_{r,TMD}^{1/3} - 1\right) \frac{\rho_0}{\rho_{TMD}} + 1, \tag{1.5}$$

where ρ_0 is the powder density and ρ_{TMD} is the theoretical maximum density (TMD). Throughout this work, powder density, charge density, and bulk density are used interchangeably. In the context of a crystalline explosive material, the TMD is the crystal density.

It is clear from Eq. (1.5) that permittivity is a function of density. In a shocked porous material, the advancing shock front creates a dielectric discontinuity which reflects microwaves [55]. If chemical reaction occurs, e.g. in detonating explosives, the advancing shock front acts as a conductor [57]. The reflected signal is interfered with the incident or reference microwave signal, resulting in a fringe pattern. The velocity of the detonation front denoted by D is then calculated as:

$$D = \frac{\lambda_g}{2} f, \tag{1.6}$$

where λ_g is the interference wavelength of the microwave interference signal in the explosive material and f is the frequency of the waveform. The interference wavelength is found from

$$\lambda_g = \frac{\lambda_0}{\sqrt{\epsilon_r - (\lambda_0/\lambda_c)^2}}. \tag{1.7}$$

In a circular waveguide, the lowest mode that will propagate is the TE_{11} is the lowest frequency that can be propagated [54]. Knowing the speed of light in free space and solving for wavelength using cutoff frequency yields the equation $\lambda_c = 3.413R$ as the cutoff wavelength for a circular wave-guide. In Eq. (1.7), λ_c is the cutoff wavelength, which represents maximum wavelength can be propagated in the waveguide and λ_0 is the free space wavelength. The free space wavelength is defined as $\lambda_0 = c/f$, where

F is the frequency of the microwaves generated by the source.

Cawsey *et al.* specified a guideline that for a circular charge geometry the frequency of the source should be inside the range

$$\frac{2c}{3.413d\sqrt{\epsilon_r}} \le f \le \frac{2c}{2.613d\sqrt{\epsilon_r}}, \tag{1.8}$$

where c is the speed of light, d is charge diameter, and ϵ_r is the permittivity of the explosive. Cook *et al.* attributed the low quality of their results to the propagation of multiple modes in their charges. Using Cawsey's criterion, it is evident that the source frequency was significantly outside the limit at which the second mode would be propagated within the waveguide [54,58]. The frequency term in Eq. (1.6) can be found by peak-picking, which is a simple method of determining detonation velocity from an MI waveform. However, this technique offers poor spatial resolution since the number of velocity points obtainable from MI data is limited to the number of successive peaks in the waveform.

Strand *et al.* demonstrated the use of phase angle to obtain greater spatial resolution. In their study, they used a microwave network analyzer to obtain the phase angle and related this to velocity using the relation:

$$v(t) = \frac{\lambda_g}{4\pi} \frac{\mathrm{d}\phi}{\mathrm{d}t}, \tag{1.9}$$

where $\phi(t)$ is the phase velocity [59].

1.3.2 Literature Review of MI

Cook *et al.* represents one of the earliest reported uses of microwave interferometry as a detonation diagnostic. The authors used a free-field 9.4 GHz microwave source in a Michelson interferometer configuration to measure detonation velocities of 5 cm charges [58]. In their study, Cook *et al.* interpreted their results as a Doppler shift being applied to the incident microwave signal as a result of the propagating det-

onation front [58]. Cawsey *et al.* also used microwave interferometry to measure the detonation velocity of an explosive [54]. The basic guidelines for fielding MI in detonation experiments are outlined in Cawsey *et al.* They also demonstrated the use of MI for tracking run distance to detonation, which shows potential for tracking time-dependent detonation phenomena. Additionally, Cawsey *et al.* discussed the sensitivity of MI to density gradients.

MI has also been used for measuring propellant burn rates. As mentioned above, Strand *et al.* achieved improved spatial resolution with microwave interferometry on propellants. Strand *et al.* used the phase shift method from a previous publication to demonstrate the application of microwave interferometry to analyzing oscillatory combustion behavior in solid propellants [60].

McCall *et al.* incorporated a quadrature mixer into an MI system and used this to obtain the instantaneous phase. The quadrature mixer yielded two waveforms that had a 90° phase offset from one another. As a result, the two waveforms S_1 and S_2 could be written as

$$S_1 = A_1(t) \sin(\phi(t)) \tag{1.10}$$

and

$$S_2 = A_2(t) \cos(\phi(t)). \tag{1.11}$$

where A_1 and A_2 represented the respective time-varying amplitudes of the two signals [61]. McCall *et al.* observed that if A_1 and A_2 were equal, the phase could be calculated as

$$\phi = \tan^{-1}\left(\frac{S_2}{S_1}\right). \tag{1.12}$$

McCall *et al.* also showed that the calculated position of the detonation front obtained using their method agreed with data obtained from time-of-arrival pins but

with superior spatial resolution [61]. Furthermore, the position data agreed with that obtained with a streak camera. This result was significant in that it demonstrated the ability of MI to yield comparable results to that of a streak camera, showing its versatility particularly in experiments where optical access was not possible.

A major question of MI was the cause of the reflectivity of microwaves both in condensed phase detonation and propellant deflagration. Early work theorized that ionization or plasma in the shock front caused these reflections [58]. Essentially, the shock or reaction front acts as a conductor which reflects microwaves. Anicin *et al.* examined interference waveforms from burning polyurethane strand and found that the amplitudes were below what would be expected of microwave reflecting off of a conductive surface which led them to conclude that the reflection was due to changing dielectric properties at the solid-gas interface [62]. The authors also concluded that ionization in shock fronts was not the cause of microwave reflections seen in detonation experiments. However, Glancy *et al.* analyzed shock compaction of an energetic material using microwave interferometry, continuing previous work with inert materials and found that compression alone of the powder could not account for the increase in microwave reflections and concluded that ionization was also contributing [57]. The authors inferred the from the microwave amplitudes that during buildup to detonation, ionization was concentrated in local regions in hot spots and the distribution of ions or plasma became uniform once detonation was steady [57]. This confirms conclusions of other researchers that shock-to-detonation and deflagration-to-detonation transition is highly dependent on energy localization [63].

As mentioned previously, the incorporation of a quadrature mixer to yield a second phase-shifted channel represented a significant improvement in the spatial resolution that could be achieved with MI. The majority of work with microwave interferometry however has been directed towards using it to study other phenomena besides steady detonation (e.g. buildup to detonation) and fielding higher-frequency interferometers.

Cawsey *et al.* demonstrated the possibility of tracking run distance to detonation with MI [54]. Rae *et al.* fielded a free-field interferometer to measure detonation velocity and run-to-detonation distance. In their study, the authors used a high-gain horn that was at a standoff distance from the explosive, allowing for unperturbed interrogation of the detonation event [64]. They obtained a position-time plot using the quadrature analysis method that showed steady behavior from the start of the detonation event in the sample charge [64]. The presence of the aluminum foil between the PBX 9501 booster and test sample along with the polytetrafluoroethylene (PTFE) plate at the end of the charge enabled accurate identification of the start and end of the detonation event in the sample [64]. Taking the integral of Eq. (1.9) with respect to time over the time interval of the detonation event and setting this equal to known charge length, the authors calculated the dielectric permittivity to be 3.84, which was comparable to a value of 3.52 measured at 24 GHz for PBX 9404, another HMX-based explosive [64]. From their data, the authors calculated the detonation velocity of PBX 9501 to be 8.68 ± 0.01 km/s, which was comparable to the velocity predicted by CHEETAH v6.0, which was 8.71 km/s [64]. The authors' result was also significant because instead of using a measured permittivity, the authors determined permittivity from the measurement data. It should be noted however that the authors' charge diameter was outside the frequency limits determined using Cawsey *et al.* though this did not appear to compromise the quality of the authors' data. [54,64].

Tringe *et al.* also used MI to characterize shock-to-detonation transition (SDT) and in addition deflagration-to-detonation transition (DDT) [56]. In their SDT experiments, the authors observed that the MI signal amplitude increased and then decreased shortly before transition to detonation, which was indicative of hot spot growth [56,63]. This result was in agreement with the findings of Glancy *et al.* [57]. In both cases, MI overestimated the shock velocity relative to time-of arrival gauges fielded for both experiments (ionization pins for DDT and manganin gauges for SDT)

which is attributable to inaccuracy in determination of the dielectric constant [56]. Luther *et al.* used MI to measure shock and particle velocities in Teflon [65]. While the results were preliminary as noted by the authors, the authors' work demonstrated the possibility of using MI for such a measurement [65]. Belskii *et al.* performed similar experiments and also demonstrated the use of MI to analyze plate impact by a detonation wave [66]. A major question with using MI for measuring particle velocities is the time resolution that could be obtained with this measurement.

Various researchers have demonstrated the use of MI to observe and analyze transient phenomena relevant to detonation including SDT and detonation buildup. MI has also been used to study detonation failure, particularly for non-ideal explosives (e.g. ammonium nitrate based explosives). The longer reaction zone lengths characteristic of non-ideal explosives coupled with weaker shock fronts makes application of MI challenging for this type of application [67,68]. In experiments with mixtures of ammonium nitrate and mineral oil, Janesheski *et al.* used MI with the quadrature analysis method for measuring detonation velocity and obtaining shock front position [67]. However, the relative error in the position calculation was 2-5%. Kittell *et al.* compared the results of quadrature analysis and time frequency analysis on low-quality MI data from a non-ideal explosive and concluded that that because of their superior resolution, time frequency analysis methods were better suited for capturing transient events within these types of detonation experiments [68].

A 35 GHz custom microwave interferometer was constructed for characterizing detonation in non-ideal explosives [67]. Because it was readily available, this diagnostic was fielded for measuring detonation velocities of cocrystals and their corresponding physical mixtures, the results of which are presented in this work. The system is a heterodyne microwave interferometer in which a 27 GHz and 8 GHz signal are combined using a combination of mixers, circulators, filters, etc. to produce a 35 GHz signal. The quadrature mixer produces a signal phase-shifted by 90°. The in-phase

and quadrature signals are independently interfered with the reflected signal, yielding two output signals.

1.4 Detonation Dynamics

A detonation wave is a self-sustaining, steadily propagating shock-wave whose energy comes from chemical reactions initiated by compression due to detonation products [69]. In the context of condensed phase explosives, the detonation front travels at a velocity of several kilometers per second. Detonation events happen over fast timescales, on the order of microseconds.

Detonations are analyzed using the Rankine-Hugoniot (R-H) jump equations [69,70]. An idealized detonation front is shown in **??**. The shock front is assumed to be planar and one-dimensional. The R-H equations are the conservation equations written

$$
\begin{array}{c|c}
u & u_0 \\
P & P_0 \\
\rho & \xrightarrow{D} \rho_0 \\
E & E_0
\end{array}
$$

across the shock front [70]. The detonation front is analyzed from a shock-attached reference frame as shown in Fig. 1.7. In this frame, the un-reacted material propagates into the discontinuity at velocity $u_0 - D$ and exits at velocity $u - D$. The velocity of the unreacted material is zero.

$$
\begin{array}{c|c}
-D & u - D \\
P_0 & P \\
\rho_0 & \rho \\
E_0 & E
\end{array}
$$
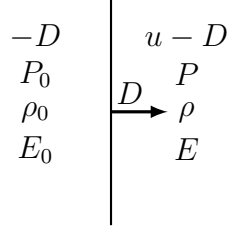
Figure 1.7. Detonation front diagram with shock-attached reference frame.

The equation for conservation of mass is [69]:

$$\rho_0 D = \rho(D - u), \tag{1.13}$$

where ρ_0 is unreacted material density, u is the particle velocity of the shock products, D is the shocked velocity, and ρ is the density of the shocked material. The equation for conservation of momentum is:

$$\rho(D - u)^2 - \rho_0 D^2 = P_0 - P. \tag{1.14}$$

Using Eq. (1.13), Eq. (1.14) reduces to:

$$\rho_0 u D = P - P_0. \tag{1.15}$$

Conservation of energy across the shock front is

$$\rho_0 D \left[(E - E_0) + \frac{1}{2}[(D - u)^2 + D^2] \right] = P_0 D - P(D - u). \tag{1.16}$$

From Eq. (1.13), it can be seen that

$$u = D \left(1 - \frac{\rho_0}{\rho} \right), \tag{1.17}$$

which implies that the particle velocity of the shocked products cannot exceed the velocity of the shock front. Using Eq. (1.17), u is substituted into the momentum and energy balances. The momentum balance becomes

$$\rho_0 D^2 \left(1 - \frac{\rho_0}{\rho} \right) = P - P_0. \tag{1.18}$$

The energy balance becomes

$$E - E_0 = \frac{1}{2}(P + P_0)(v_0 - v), \tag{1.19}$$

where v represent specific volume, the reciprocal of density [69]. Beginning at an initial state, defined by the appropriate state variables, e.g. p_0 and ρ_0, Eq. (1.18) represents the locus of post-shock states (pressure and specific volume) for which the equations of mass and momentum are satisfied. Eq. (1.19) specifies locus of post-shock states for which conservation of energy is satisfied, which is known as the Hugoniot. The reactant and product Hugoniot curves are shown in Fig. 1.8. In the
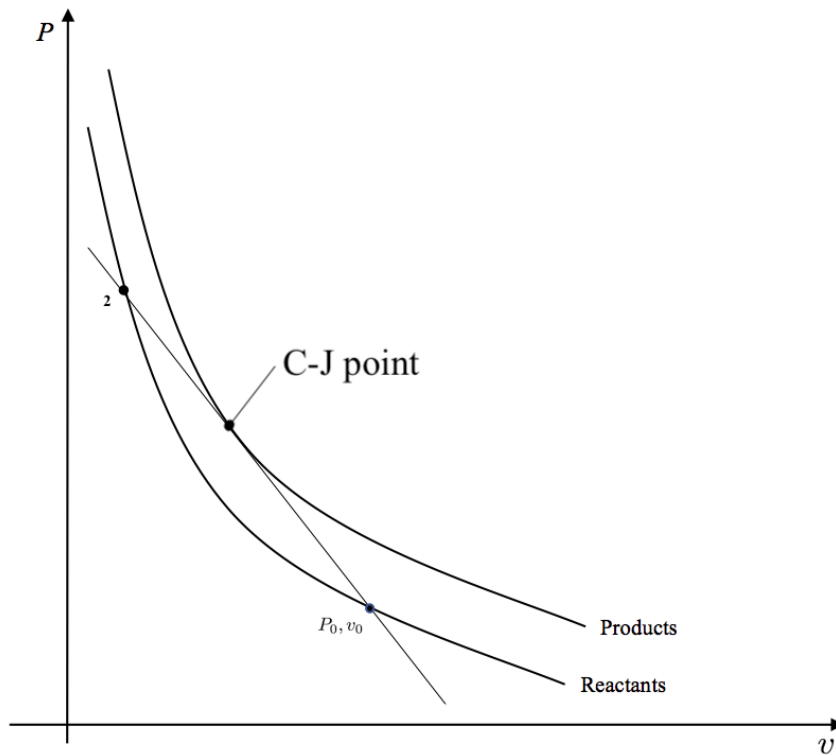

Figure 1.8. Product and reactant Hugoniot curves.

context of detonation, the reaction zone is the space between the post-shock state of the reactants denoted by point 2 in Fig. 1.8 and the point of tangency between the Rayleigh line and the product Hugoniot. Eqs. (1.13) to (1.16) are not sufficient to compute the detonation velocity. The Chapman-Jouguet (C-J) condition states that

the detonation velocity is the sum of the local speed of sound and particle velocity [71].

The C-J isentrope is derived from the equation of state of the products. At the C-J point, the Hugoniot and the C-J isentrope have the same derivative, meaning the Rayleigh line is tangent to both [71].

The simplest theory of detonation, known as C-J detonation, assumes that the reactants convert to the products instantaneously, implying that the reaction zone has zero thickness. At the C-J point, chemical and thermodynamic equilibrium are attained.

Given a fundamental thermodynamic relation of the form $E(V, S)$, where E is internal energy, V is volume, S is entropy, equations of state (EOS) are defined as partial derivatives of the fundamental relations. For example, pressure is defined as [70]

$$\frac{\partial E}{\partial V}_S = -p. \tag{1.20}$$

Given the Gibbs free energy of a system of the form $G(T, p, n)$, the chemical potential μ_i is defined as

$$\mu_i = \frac{\partial G}{\partial n_i} \tag{1.21}$$

Attaining chemical equilibrium is equivalent to minimizing the Gibbs free energy function, which states that [72]

$$\mathrm{d}G = \sum \mu_i \, \mathrm{d}n_i = 0. \tag{1.22}$$

Thermochemical codes for predicting C-J detonation properties compute the equilibrium state by solving Eq. (1.22). Using the computed equilibrium state, the code uses the equation of state to obtain the C-J isentrope. A number of equations of state have

been developed. One of the earliest equations of state was the Becker-Kistiakowsky-Wilson (BKW) EOS, an empirical relationship of the form

$$\frac{pV}{nRT} = 1 + xe^{\beta x}, \tag{1.23}$$

where x and β are empirically determined parameters [73]. A drawback of the BKW EOS is that it fails to account for attractive forces between gaseous molecules. The Jacobs-Cowperthwaite-Zwisler (JCZ) EOS is a more sophisticated EOS that accounts for intermolecular interactions of the gaseous detonation products [74]. Predictions of detonation properties in a thermochemical code known as CHEETAH make use of primarily the JCZ EOS. In this work, the JCZ EOS was used for CHEETAH calculations unless specified otherwise.

Using a suitable equation of state along with the conservation laws, one can arrive at the C-J state and compute detonation velocity, pressure, temperature etc. as is done with thermochemical codes. As an alternative, however, one can predict detonation properties by looking at the relative effects that various properties of the explosive have. It has long been known that the relationship between detonation velocity and loading density for a given explosive can be represented quite accurately as a linear relationship of the form [75, 76]

$$D = a_1 + a_2\rho_0, \tag{1.24}$$

where A and B are constants. Having performed thermochemical predictions for various explosives in a range of loading densities using a code known as RUBY, Kamlet *et al.* identified the product composition and heat release in addition to density as the three key factors that have the most pronounced effect on detonation velocity [76]. A phenomenological scaling relationship of the form

$$\xi = NM^{1/2}Q^{1/2} \tag{1.25}$$

was derived where N is the number of moles of gas produced per kilogram of explosive, M is the average molecular weight of the gaseous products in g/mol, and Q is the heat of detonation in cal/g. The heat of detonation is defined as

$$Q = \left(\sum \Delta H_f^\circ\right)_{\text{products}} - \left(\sum \Delta H_f^\circ\right)_{\text{reactants}}, \tag{1.26}$$

where ΔH_f° is the heat of formation. Using Eqs. (1.25) to (1.26), Eq. (1.24) was rewritten as

$$D = A\xi^{1/2}(1 + B\rho_0), \tag{1.27}$$

where A and B were empirically determined to be 1.01 and 1.3, respectively [76]. From Eq. (1.27), it can be seen that the most dominant parameter affecting detonation velocity is the loading density. This result supports the general trend observed for explosives that denser explosives typically have higher detonation velocities. However, the presence of other terms that affect detonation velocity can explain observed differences for two energetic materials of comparable loading density. For example, HMX at a loading density of 1.89 g/cm^3 detonates at 9.11 km/s while TATB at a loading density of 1.86 g/cm^3 detonates at 7.62 km/s, a difference of about 20% [77]. Using Eqs. (1.26) to (1.27) with enthalpy of formation data from [77] and assumed detonation products of the form shown in Eq. (1.28) [76],

$$C_aH_bN_cO_d \rightarrow \left(\frac{1}{2}c\right)N_2 + \left(\frac{1}{2}b\right)H_2O + \left(\frac{1}{2}d - \frac{1}{4}b\right)CO_2 + \left(a - \frac{1}{2}d + \frac{1}{4}b\right)C \tag{1.28}$$
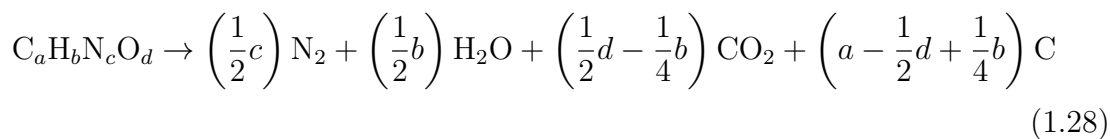
HMX is predicted to have a detonation velocity that is about 27% greater than that of TATB. While the predicted difference is higher than the measured difference, the measured and predicted differences are qualitatively similar. Since loading densities are relatively close, the difference is attributable to the superior oxygen balance and higher heat of formation for HMX. In this manner, the contribution of properties affecting detonation can be seen.

An improvement over the classical model of detonation is the Zeldovich-von Neumann-Doering (ZND) model, the advancing shock front first compresses the unreacted explosive to the von Neumann spike state [11]. Chemical reactions occur after this state is attained, with the products expanding to the C-J state. Essentially, the ZND model permits reaction kinetics, resulting in a finite reaction zone thickness. However, throughout this work, only the classical model of detonation is applied.

2. EXPERIMENTAL METHODS

2.1 Sample Preparation

In this work, the detonation velocities of cocrystals and corresponding physical mixtures were compared at the same loading density. It is well-known that minimization of density gradients is critical to obtaining high-quality MI data. It was therefore decided to press all sample materials incrementally to a loading density of 1.4 g/cm^3 as an additional measure to avoid density gradients.

A cutaway view of the test samples is shown in Fig. 2.1.
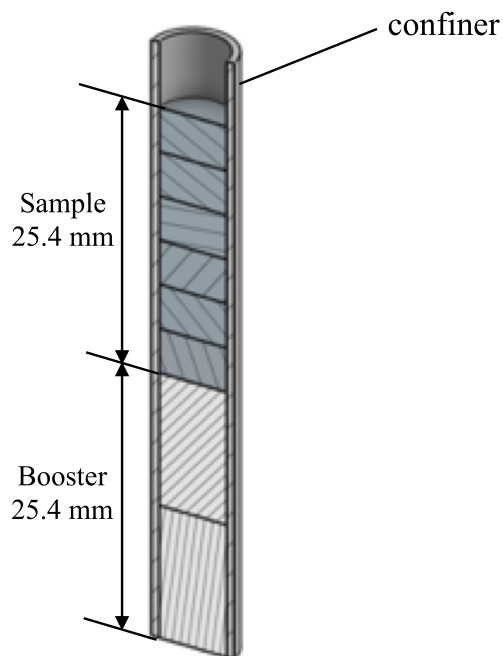
Figure 2.1. Cutaway view of test samples.

In order to initiate the sample material to a steady detonation velocity over a minimal distance, a booster charge of neat HMX, Grade B, Class 3 was to pressed to nominally 85% TMD in the first 25.4 mm of the confiner. The booster was pressed in two increments using 12.7 mm aluminum spacers machined to a tolerance of 25.4 μm. For the ADNP/DAF cocrystal shots, PBX 9501 pressed to 90% TMD was used as the booster material.

A piece of 25 μm foil was pressed into the confiner on top of the booster charge in order to delineate the start of the detonation of sample material on the MI waveform. The sample material was pressed in six increments using aluminum spacers machined to a height of 4.24 ± 0.025 μm. To minimize the uncertainty in diameter, precision ground stainless steel tubes from McMaster-Carr (6100K148) having an inner diameter of 6.52 mm and wall thickness of 0.71 mm were used. These tubes were measured using gage pins accurate to 25 μm. The confiners were machined to a height of 57.15 ± 0.025 mm. A picture of the confiners used in this work is shown in Fig. 2.2. An analysis of measurement uncertainty will be presented in detail in a later section.
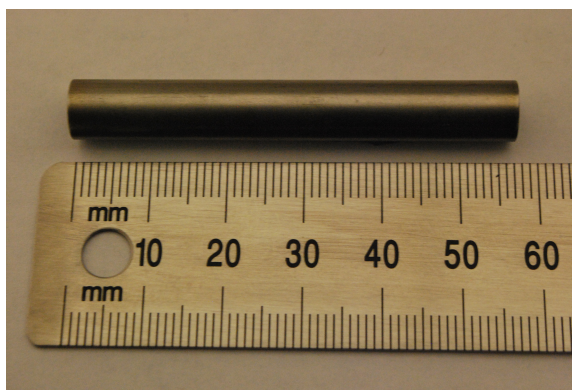
Figure 2.2. Stainless steel confiner.

The HMX/CL-20 and MDNT/CL-20 cocrystal were both provided by Picatinny Arsenal and were prepared using the resonant mixing method [46,47]. The orthorhombic CL-20/HP solvate was prepared by dissolving CL-20 in acetonitrile and precipitating the solvate form using hydrogen peroxide (>95% purity). The synthesis of the CL-20/HP solvate was done in collaboration with Dr. Jonathan C. Bennion (formerly at University of Michigan, now at Army Research Laboratory) and Ren Wiscons (University of Michigan).

The ADNP was prepared by Ren Wiscons and Rosalyn Kent (University of Michigan) and was synthesized according to the method described in Klapotke *et al.* [78] which is briefly described herein. The starting material is 4-chloropyrazole. A nitration reaction with 65% oleum adds two nitro groups to the pyrazole ring. An amination reaction is then performed to substitute the chlorine atom with an amino group. The 3,4-diaminofurazan (DAF) (97% purity) was purchased from Sigma Aldrich and used as is. The ADNP/DAF cocrystal was prepared by adding ADNP and DAF in equal molar amounts to a glass vial and then shaking the vial on an orbital shaker for several days.

2.2   Detonation Experiment

A diagram of the detonation experiment is shown in Fig. 2.3. A Teledyne RISI RP-502 Exploding Bridgewire (EBW) detonator is initiated using a capacitive discharge unit (CDU). A 6.35 mm (1/4 in.) polytetrafluoroethylene (PTFE) rod is inserted into the confiner such that it is in contact with the sample material. The other end of the rod is inserted into a WR-28 waveguide on the 35 GHz microwave interferometer. The in-phase and quadrature channels on the MI are connected to the first two channels on a Tektronix DPO4034 oscilloscope. A fiber optic cable is inserted at the
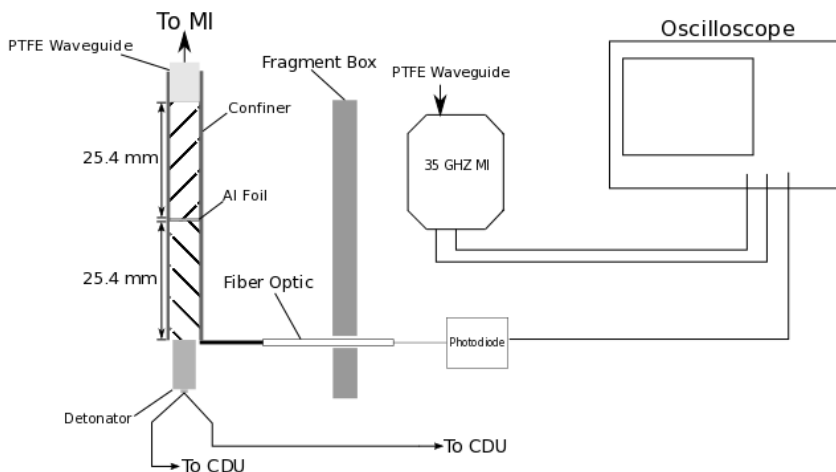
Figure 2.3. Diagram of detonation experiment.

junction of the charge and the EBW. This fiber optic cable is connected to a Thorlabs DET10A photodetector. This is connected to the third channel on the oscilloscope and is used to trigger the shot.

For the ADNP/DAF experiments, a linear current sensor (Honeywell CSLA1DJ) was used in lieu of a fiber optic probe as the trigger signal for the oscilloscope. The current sensor detected the change in current from discharging the capacitor in the CDU. In this configuration, the fiber optic cable was used to track detonator breakout.

2.3 Bomb Calorimetry

For the HMX/CL-20 and MDNT/CL-20 cocrystals, which were provided by Picatinny Arsenal, bomb calorimetry experiments were performed at Picatinny Arsenal using a Parr Instruments Calorimetric Thermometer 6772 and Semimicro Calorimeter 6725 with a 1109A Semi-Micro Oxygen Bomb. The calorimeter was calibrated using a benzoic acid standard in order to determine the heating value of the calorimeter. The nominal amount of material used for each measurement was 0.1 g.

Bomb calorimetry experiments were performed on the CL-20/HP solvate at Purdue University using a Parr 1281 bomb calorimeter. The samples were nominally 0.3 g. No spike was used. No correction for nitric acid was made in the gross heat of combustion calculations. Using the gross heat of combustion and temperature from the calorimetry measurement, the enthalpy of combustion in kJ/mol denoted as ΔH_c is defined as:

$$\Delta H_c = -\left(Mu(4.186 \times 10^{-3}) + \Delta nRT\right), \tag{2.1}$$

where M is the molecular weight, u is the gross heat of combustion in cal/g measured by the bomb calorimeter, Δn is the net moles of gas produced, R is the universal gas constant in J/kg mol and T is temperature.

For a CHNO explosive with the formula $C_xH_yN_zO_w$ undergoing complete combustion, the net moles of gas produced Δn is:

$$\Delta n = -\frac{y}{4} + \frac{z}{2} + \frac{w}{2}. \tag{2.2}$$

The enthalpy of formation denoted as ΔH_f° is computed as:

$$\Delta H_f^\circ = \frac{y}{2}\Delta H_{f,\text{H}_2\text{O}(l)}^\circ + x\Delta H_{f,TCO_2}^\circ - \Delta H_c. \tag{2.3}$$

A table showing materials used and other information such as TMD, relative permittivity etc. is shown in Table 2.1.

2.4 Analysis Methods

A sample interference waveform is shown in Fig. 2.4 with the in-phase and quadrature signals denoted as CH1 and CH2, respectively. To analyze the shot, the first step was

Table 2.1. Material data .

| Material	TMD (g/cm^3)	ΔH_f° (kJ/mol)	Notes
HMX	1.905	75	[1]
CL-20	2.044	377	[16]
CL-20/HP Solvate	2.033	748	[79]
HMX/CL-20 CC	1.945	928	ARDEC/Picatinny
HMX/CL-20 PM	2.007	829	Calc.
MDNT/CL-20 CC	1.883	1025.19	ARDEC/Picatinny
MDNT/CL-20 PM	1.929	499	Calc.
ADNP	1.9	-0.837	[36]
DAF	1.61	72	[80]
ADNP/DAF CC	1.698	71.2	Calc.
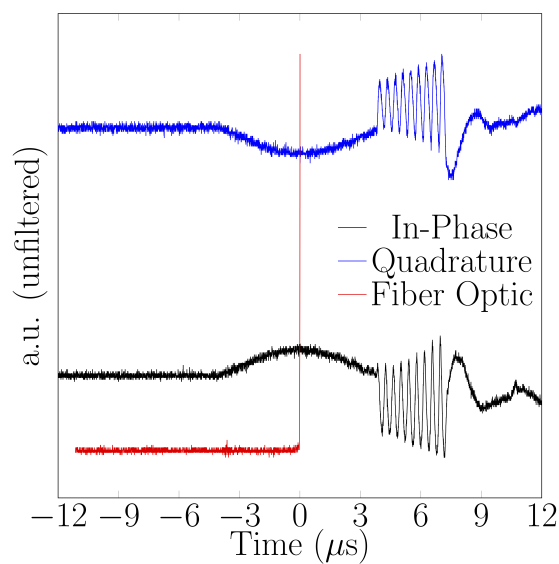
Figure 2.4. Unfiltered data from microwave interferometer.

to identify the start and end times for the detonation event. This was done by fitting a function of the form:

$$V(t) = A(t)\sin(2\pi f t + \Phi) + c, \tag{2.4}$$

where $V(t)$ is the value of the signal at time t and $A(t)$ is the amplitude at time t. The parameters f, ϕ and c are adjusted to fit the data. First, an initial estimate was made for the start and end times of the detonation event. The portion of the interference waveform falling within this time window was selected. A second-order Butterworth low-pass filter was then applied to the data. The two signals were then normalized such that the amplitudes were between $[-1, 1]$.

For the HMX and MDNT/CL-20 cocrystal shots, $A(t)$ was taken to be a constant. The Levenberg-Marquardt (LM) algorithm was then applied to determine the fitting parameters that would best fit the data.

For the HMX/CL-20, CL-20/HP solvate and ADNP/DAF shots, $A(t)$ was taken to be an exponential function of the form ae^{bt}, such that Eq. (2.4) can be written as:

$$V(t) = ae^{-bt}\sin\left(2\pi f t + \Phi\right) + c. \tag{2.5}$$

To improve the efficiency of the curve-fit routine, the LM algorithm was used only to find a and Φ. To calculate b, first

$$\ln\left[\frac{V(t_{i+1}) - V(t_i)}{t_{i+1} - t_i}\right] \tag{2.6}$$

was calculated, where $V(t_{i+1})$ and $V(t_i)$ the amplitudes of two successive peaks with t_{i+1} and t_i being the times corresponding to the peaks. The value of b was taken as the average of the values found with this expression. The value of f was taken to be the average frequency determined by peak-picking. The value of c was taken as the average value of the signal after normalizing.
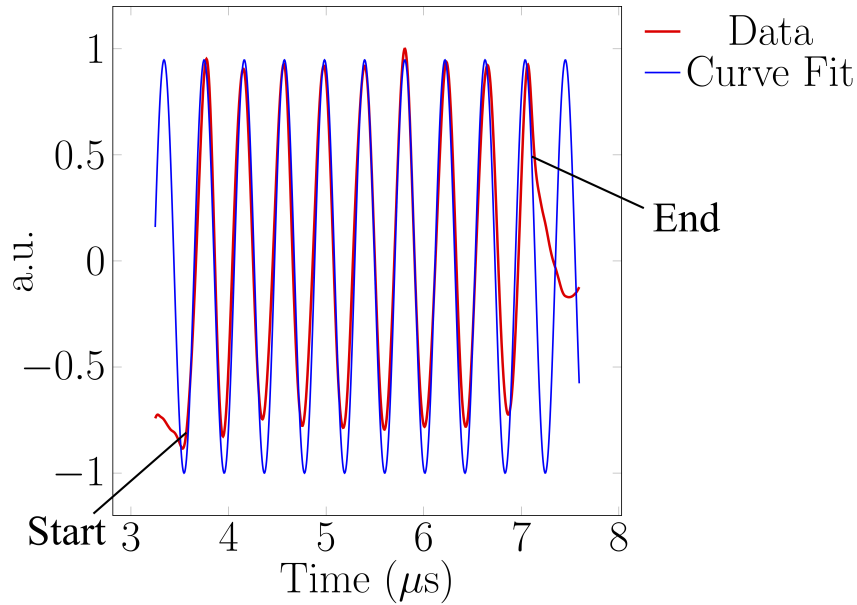
Figure 2.5. Sample curve-fit to filtered and normalized data.

A curve-fit obtained according Eq. (2.4) overlaid with the filtered and normalized data forn HMX detonation test is shown in Fig. 2.5. It can be seen in Fig. 2.5 that there is a point at which the beginning of the waveform matches the fitted sinusoid and likewise, there is a point on waveform at which the signal diverges from the fitted sinusoid. A range of possible values for both the beginning and end of the waveform was identified. The start time and end times were taken to be the values within the selected ranges that were below the threshold deviation. A similar process was followed for the quadrature signal. The averaged start time and averaged end time between the in-phase and quadrature signals was computed and used as the estimate of the time range of the detonation event.

After cutting the waveform based on the estimated start and end-times of the detonation event, a light second-order high-pass Butterworth filter was applied to remove any DC offset. A second-order low-pass Butterworth filter was then applied in order to attenuate high-frequency noise.

With an ideal quadrature detector system, the gain in the in-phase and quadrature signals would both be unity. The waveform is then normalized by performing the operation

$$V_n(t) = \frac{1}{V_{f,\max}} \left(V_f(t) - \bar{V}_f\right), \tag{2.7}$$

where $V_n(t)$ represents the normalized signal, $V_{f,\max}$ represents the maximum value of the filtered signal and $\bar{V}_f$ represents the mean value of the filtered signal $V(t)$. The result of performing the operation described in Eq. (2.7) is shown in Fig. 2.6. It can be seen that normalization with a single parameter according to Eq. (2.7) will not yield a signal with constant amplitudes. The effects of unequal signal gain and zero offset remain in the waveform. The waveform shown in Fig. 2.6 has the additional effect of decreasing signal loss as the shock front reaches the signal source although this effect is a characteristic of the sample material rather than an imperfection of quadrature interferometers.

To mitigate the effect of unequal signal gain, a Hilbert transform is first applied to the two normalized signals. The Hilbert transform is a linear operator that generates an orthogonal complement to a given signal [81]. The original signal and its harmonic conjugate, which is orthogonal to the original signal, form the real and imaginary parts of the transformed signal such that the absolute value of the transformed signal gives the envelope function of the original signal. Each point in the normalized waveform is re-normalized to the envelope function.

After the above normalization, additional nonidealities remain in the data due to channel nonorthogonality and zero offset [82]. The combined effect of these nonidealities can be modeled as translation, distortion, and rotation of a unit circle [82]. A Lissajous curve of the raw quadrature data would show up as a distorted ellipse. The Lissajous curve of a shot with HMX is shown in Fig. 2.7 wherein the in-phase signal is plotted on the x-axis and the quadrature signal is plotted on the y-axis. The
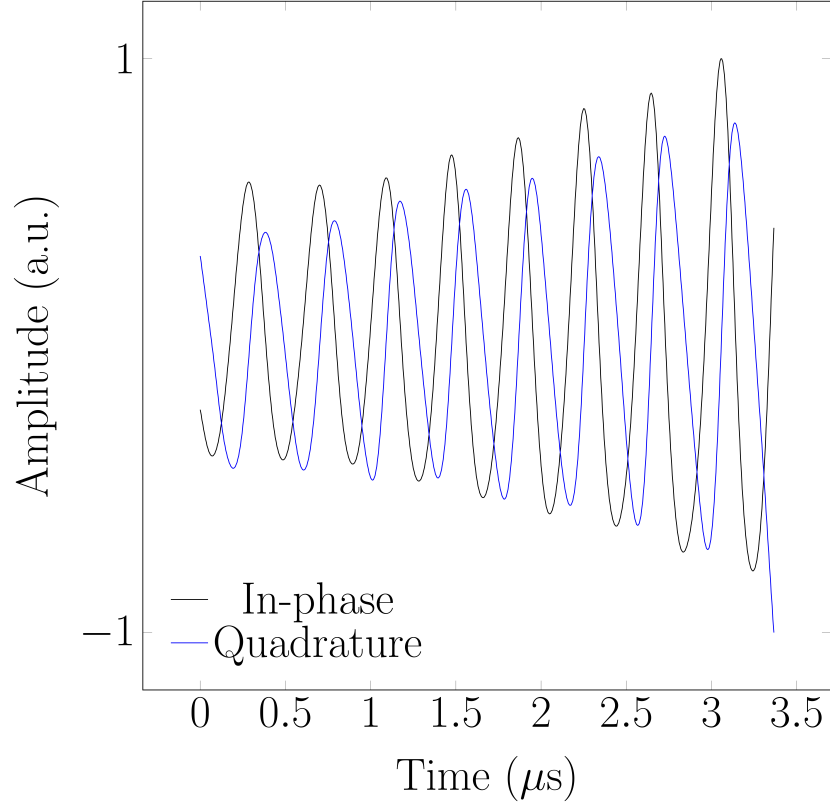
Figure 2.6. Filtered waveform normalized according to Eq. (2.7).

equation of the ellipse is

$$
\begin{bmatrix} V_1 \\ V_2 \end{bmatrix} = \mathbf{Q}(\alpha) \begin{bmatrix} a & 0 \\ 0 & b \end{bmatrix} \begin{bmatrix} V_{1c} \\ V_{2c} \end{bmatrix} + \begin{bmatrix} z_x \\ z_y \end{bmatrix},
\tag{2.8}
$$

where $\mathbf{Q}(\alpha)$ represents the rotation matrix as a function of angle α, a and b are respectively the major and major axes of the ellipse, V_{1c} and V_{2c} are the corrected signals, and z_x and z_y are the coordinates of the center of the ellipse [83]. The parameters α, a, b, z_x, and z_y are obtained by fitting the waveform data (V_1 and V_2) to an ellipse described by the equation [68, 83]

$$
\begin{bmatrix} x \\ y \end{bmatrix} = \mathbf{Q}(\alpha) \begin{bmatrix} a & 0 \\ 0 & b \end{bmatrix} \begin{bmatrix} \cos\theta \\ \sin\theta \end{bmatrix} + \begin{bmatrix} z_x \\ z_y \end{bmatrix}.
\tag{2.9}
$$
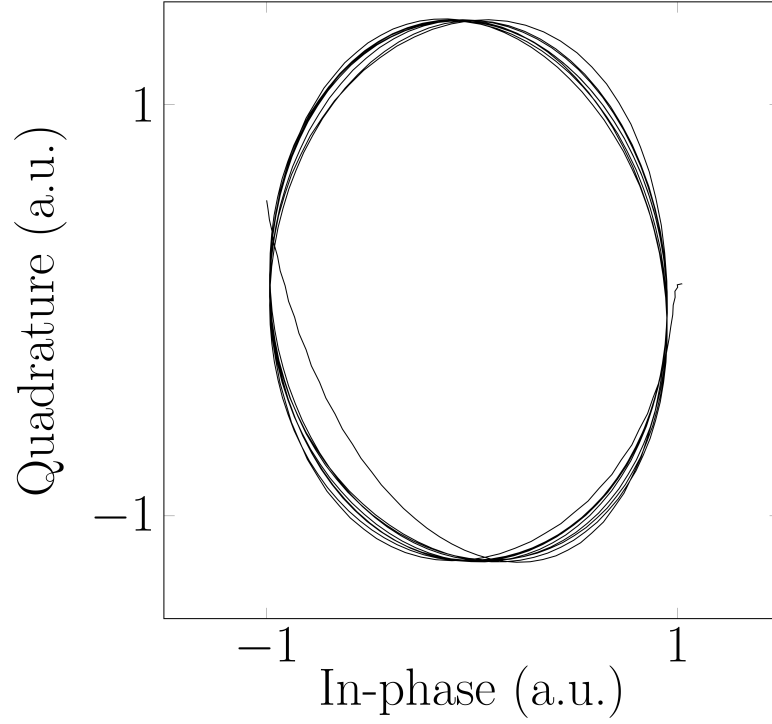
Figure 2.7. Lissajous curve of MI waveform data after normalization to envelope function.

After substituting the parameters to fit the data to an ellipse, Eq. (2.8) is solved for $[V_{1c}; V_{2c}]$ to obtain the corrected signals. The amplitudes were then normalized between $[-1, 1]$. The Lissajous curve after correcting the signals according to Eqs. (2.8) to (2.9) is shown in Fig. 2.8 For all shots presented in this work, the quadrature method was used to determine the detonation velocity. The instantaneous phase was calculated as:

$$\phi(t) = \tan^{-1}\left(\frac{V_{2c}(t)}{V_{1c}(t)}\right), \qquad (2.10)$$

where V_2 is the in-phase signal and V_1 is the quadrature signal. The corrected quadrature signals obtained using Eqs. (2.8) to (2.9) were used to compute the instantaneous phase. A phase unwrapping algorithm is then applied to this data to yield the in-
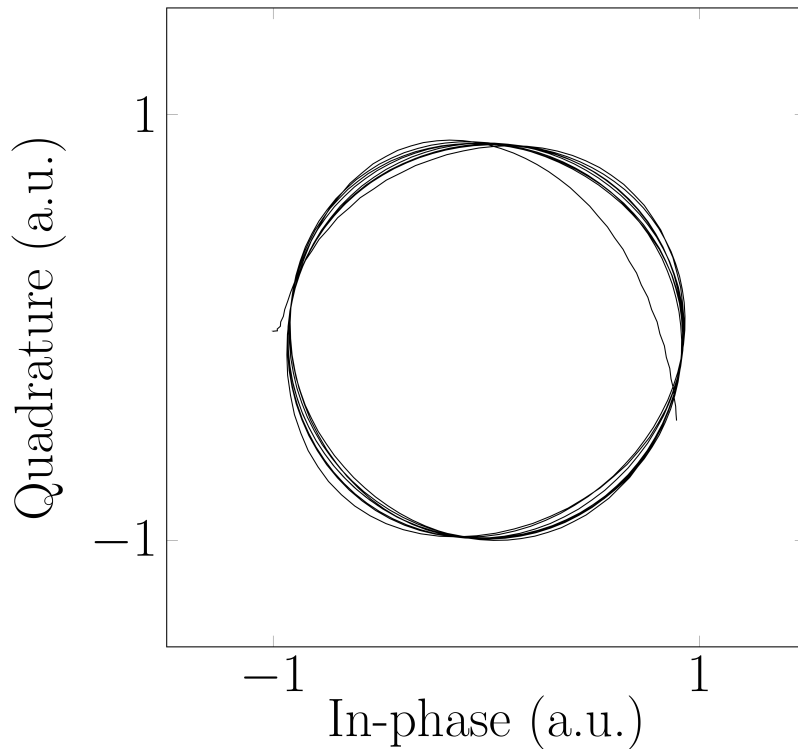
Figure 2.8. Lissajous curve of MI data after correction.

stantaneous phase. From the instantaneous phase, the detonation velocity is defined as [68]

$$v(t) = \frac{\lambda_g}{4\pi} \frac{\mathrm{d}\phi}{\mathrm{d}t}. \tag{2.11}$$

Defining $v(t)$ in Eq. (2.11) as $\mathrm{d}x/\mathrm{d}t$ and integrating both sides over the entire waveform yields position as a function of time given as

$$x(t) = \frac{\lambda_g}{4\pi} \phi(t). \tag{2.12}$$

If a measured value for ϵ_r was available, this value was used to determine the interference wavelength using Eq. (1.7). The measured permittivities were determined according to the process outlined in Daily *et al.* [84]. Measured permittivities were available for HMX, CL-20, and the HMX/CL-20 cocrystal. The HMX/CL-20 cocrystal permittivity was measured by Prof. Lori J. Groven at South Dakota School of

Mines and Technology. For materials where a measured value for ϵ_r was not available, Eq. (2.12) was recast to solve for the interference wavelength. The integral of Eq. (2.11) over the duration of the detonation event was set equal to the charge length with the start of the detonation event taken to be $t = 0$. The resulting expression was

$$L = \frac{\lambda_g}{4\phi} \int_{t_i}^{t_f} \phi(t) \, \mathrm{d}t, \tag{2.13}$$

which was solved for λ_g.

3. RESULTS

3.1   Uncertainty Analysis

In a cocrystal and its corresponding physical mixture, the same molecules are present. Therefore, one would expect the difference in detonation velocity between a cocrystal and its physical mixture to be small. An understanding of smallest velocity difference resolvable with this experimental technique is necessary in order to determine whether an observed difference can be attributed to sources of stored energy in the cocrystal other than the intramolecular bonds.

Given a measured quantity W defined as fuction of parameters $X_1, X_2, \cdots X_n$, $W = \text{fcn}(X_1, X_2, \cdots X_n)$, the overall measurement uncertainty in W is defined as:

$$\frac{\Delta W}{W} = \sqrt{\sum_{i=0}^{n} \left(\frac{\partial W}{\partial X_i} \frac{\Delta X_i}{W} \right)^2}. \tag{3.1}$$

The position of the detonation front is defined according to Eq. (2.12) as

$$x(t) = \frac{\lambda_g}{4\pi} \phi(t), \tag{3.2}$$

where $x(t)$ is the position of the detonation front as a function of time. The terms λ_g and $\phi(t)$ are respectively the material wavelength and the instantaneous phase, as described previously in Eq. (1.7) and Eq. (2.10).

Therefore, the uncertainty in detonation front position is

$$\frac{\Delta x}{x} = \sqrt{\left(\frac{\Delta \lambda_g}{\lambda_g} \right)^2 + \left(\frac{\Delta \phi}{\phi} \right)^2}. \tag{3.3}$$

In Eq. (3.3), the term $\Delta \phi$ was taken to be the phase error of the quadrature mixer in the MI. This was calculated by first constructing a plot of calculated phase as a function of time for the normalized MI signals (using a single normalization parameter)
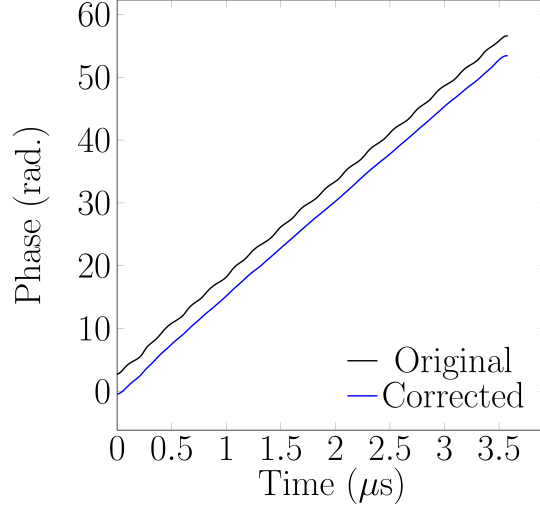
Figure 3.1. Calculated phase as a function of time using original and corrected signals.

and a similar plot using the corrected MI signals calculated according to Eqs. (2.8) to (2.9). A sample plot is shown in Fig. 3.1. It can be seen that the two lines are parallel to one another. The phase error is taken to be the mean difference in phase calculated for the two plots. The uncertainty in interference wavelength λ_g is:

$$\frac{\Delta\lambda_g}{\lambda_g} = \sqrt{\left(\left(\frac{\lambda_g}{\lambda_c}\right)^2 \frac{\Delta\lambda_c}{\lambda_c}\right)^2 + \left(\left(\frac{\lambda_g}{\lambda_0}\right)^2 \frac{\Delta\epsilon_r}{2}\right)^2}. \tag{3.4}$$

The cutoff wavelength for a circular waveguide λ_c is given by the expression $\lambda_c = 3.413 = 1.707dR$ [54]. Applying Eq. (3.1) to this expression yields $\Delta\lambda_c/\lambda_c = \Delta d/d$. The term $\Delta\epsilon_r$ is given as:

$$\Delta\epsilon_r = \sqrt{a^2 + b^2}, \tag{3.5}$$

where

$$a = 3\left(\epsilon_r^{1/3} - 1\right)\epsilon_r^{2/3}\frac{\Delta\rho_0}{\rho_0} \tag{3.6}$$

and

$$b = \epsilon_r^{2/3}\left[\left(\epsilon_r^{1/3} - 1\right)\frac{\rho_{TMD}}{\rho_0} + 1\right]^{-2}\Delta\epsilon_{r,TMD}. \tag{3.7}$$

The uncertainty in charge density denoted by $\Delta\rho_0/\rho_0$ is:

$$\frac{\Delta\rho_0}{\rho_0} = \sqrt{\left(\frac{\Delta l}{l}\right)^2 + \left(\frac{2\Delta d}{d}\right)^2 + \left(\frac{\Delta m}{m}\right)^2}. \tag{3.8}$$

It can be seen from Eq. (3.8) that the uncertainty in diameter is a major contributor to uncertainty in charge density since the quantity $\Delta d/d$ is multiplied by two.

A table of values used in Eqs. (3.3) to (3.8) is shown in Table 3.1. The average theoretical maximum density (TMD) for the analysis used in this work was assumed to be about 1.9 g/cm^3. The value for relative permittivity was taken to be 3.5 since this number was close to the permittivities for materials used in this work that had available data. Using the average TMD and relative permittivity, the material wavelength λ_g was calculated to be 5.99 mm.

The phase error was taken to be about 0.44 radians. The detonation front travels a distance equal to $\lambda_g/2$ between two successive fringes. Knowing the total length of the charge denoted by L, the total phase can be calculated as

$$\phi = \frac{2\pi L}{\lambda_g/2}. \tag{3.9}$$

Using the values given in Table 3.1, the total phase is 53.5 radians.

Using Eqs. (3.3) to (3.8), the uncertainty in position given in Eq. (3.3) was calculated to be about 1.51%. Multiplying $\Delta x/x$ by total charge length L (25.5 mm), the uncertainty in position is approximately 0.384 mm. From CHEETAH calculations on HMX, CL-20, and other materials, the detonation velocity was assumed to be about 7.5 km/s. For a nominal detonation velocity of 7.5 km/s, the time to cover the entire charge length L is calculated to be about 3.4 μs using the equation

$$t = \frac{D}{L}, \tag{3.10}$$

Table 3.1. Values used in uncertainty analysis.

Quantity	Value	Unit
Δl	25.4	μm
Δd	25.4	μm
Δm	0.006	mg
$\Delta \epsilon_r$	0.05	
$\Delta \phi$	0.44	rad
l	4.23	mm
d	6.52	mm
m	1.2	g
$\epsilon_{r,\text{TMD}}$	3.5	
ρ_{TMD}	1.9	g/cm^3
ρ_0	1.4	g/cm^3
ϕ	53.4	rad
λ_g	5.99	mm

where D is the detonation velocity. The uncertainty in detonation velocity can be calculated as

$$\frac{\Delta D}{D} = \frac{\Delta x/t}{D}, \tag{3.11}$$

where Δx is the uncertainty in position and t is the nominal time taken for the detonation front to cover the charge length at a detonation speed of about 7.5 km/s. The uncertainty in the detonation velocity computed using Eq. (3.11) is about 108 m/s.

3.2 Experimental Method Validation

HMX shots were first performed to validate the experimental method and also the method used for determining the interference wavelength. Five test samples were prepared with HMX with an average charge density of 1.405 ± 0.016 g/cm^3. It can be seen in Fig. 3.2 that the position-time curve is linear in all cases, indicating that the detonation wave was steady from the start. This indicated that the booster charge was chosen appropriately to achieve prompt initiation of the sample to a detonation. For each plot, a linear function of the form

$$x(t) = at + b \tag{3.12}$$

was fit to the position-time data where a and b are constants in units of mm/μs and $x(t)$ is the position in mm. The calculated value for a for each test sample was taken to be the detonation velocity. The standard error for the slope of a linear regression of the form shown in Eq. (3.12) is given by the equation

$$s_e = \sqrt{\frac{\frac{1}{n-2}\sum_{i=1}^{n}(x_i - \hat{x}_i)^2}{\sum_{i=1}^{n}(t - \bar{t})^2}}, \tag{3.13}$$

where $\hat{x}_i$ represents the predicted position according to Eq. (3.12) and x_i represents the position obtained from Eq. (2.12). In the denominator in Eq. (3.13), t represents

the time (independent variable) and $\bar{t}$ represents the average of the independent variable. The 95% confidence intervals (defined as $1.96s_e$) for all detonation velocities for HMX obtained with Eq. (3.12) were less than 20 m/s. This result demonstrated that treating the entire detonation event as steady was a reasonable assumption. For an
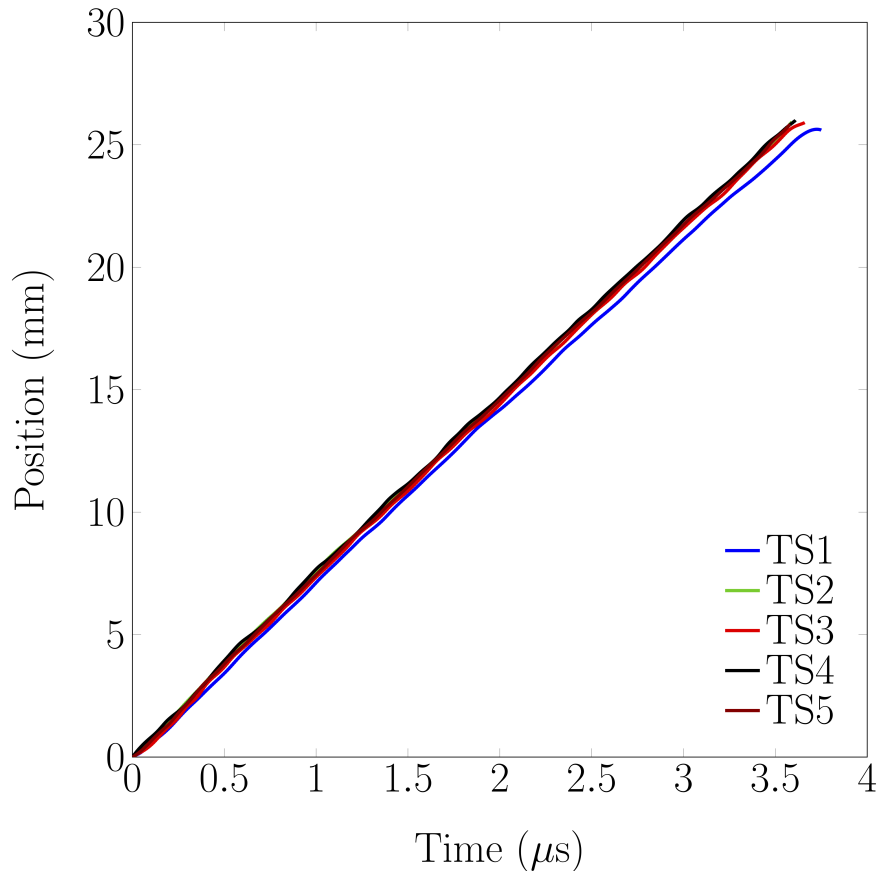
Figure 3.2. Position vs. time plots for HMX detonation tests.

average charge density of 1.405 ± 0.016 g/cm^3, the detonation velocity for HMX was found to be 7.14 ± 0.067 km/s, where ± 0.067 km/s represents the standard deviation of detonation velocity. The velocities were compared to CHEETAH using the JCZ equation of state and was found to be a complete 7.34 km/s, which is about 2.9 percent different from the measured detonation velocity. Two measurements for HMX detonated in a 25 mm diameter charge at a powder density of 1.4 g/cm^3 were reported to be 7.2 km/s and 7.3 km/s [85,86]. The detonation velocity at a number of different

powder densities was determined using CHEETAH and the resulting relationship was of the form

$$D = a\rho_0 + b, \tag{3.14}$$

where a and b are fitting constants and ρ_0 is the powder density. It was assumed that the slope of measured detonation velocities versus charge density would be the same as the value of a in Eq. (3.14). Using this relationship, the detonation velocity adjusted to a density of 1.4 g/cm^3 was determined for each test sample. In this manner, it was possible to adjust for the effect on detonation velocity of small sample-to-sample variation in pressing density. The unadjusted and adjusted detonation velocities along with comparisons to CHEETAH are shown in Table 3.2. In Table 3.2, the column denoted as (Est.) is the detonation speed determined as

$$D = \frac{L}{t_f - t_i}, \tag{3.15}$$

where t_i and t_f respectively denote the start and end times of the detonation event and L is the total length of the sample charge (excluding the booster). The columns labeled (Meas.) and (Meas., dyn.) denote detonation velocities determined according to Eq. (2.12) and Eq. (3.12), except in the latter case (i.e. (Meas., dyn.) column, the material wavelength is determined dynamically according to Eq. (2.13). The column labeled (CHEETAH) is for detonation velocities obtained in CHEETAH v7.0 using the JCZ EOS. The column labeled (Adj.) is the density-adjusted detonation velocity obtained using Eq. (1.24). The detonation velocity adjusted to a powder density of 1.4 g/cm^3 was found to be 7.14 km/s, indicating that adjusting for density effects had little effect on the mean detonation velocity. However, this reduced the standard deviation from 0.070 km/s to 0.012 km/s, indicating that the majority of the shot-to-shot variation was attributable to density variation.

The total error can be defined as

$$\delta = \sqrt{\sigma^2 + (\Delta D)^2}, \tag{3.16}$$

Table 3.2. Measured HMX detonation velocities.

Shot	ρ_0 (g/cm^3)	D (km/s)				
		(Est.)	(Meas.)	(Meas., dyn.)	(CHEETAH)	(Adj.)
1	1.377	6.79	7.02	6.92	7.27	7.12
2	1.406	7.1	7.14	7.02	7.37	7.14
3	1.414	6.96	7.16	7.04	7.39	7.13
4	1.413	7.06	7.18	7.04	7.39	7.15
5	1.416	7.12	7.18	7.09	7.41	7.14

where δ is total error, σ is shot-to-shot variation in detonation velocity or standard deviation, and ΔD is uncertainty in detonation velocity, i.e. measurement uncertainty calculated previously. Using this equation, the total error was estimated to be 109 m/s.

As mentioned previously, an alternative to the determining interference wavelength from measured permittivity is to use a dynamically determined wavelength. The effect on measurement error of calculating detonation velocity this way was examined to determine the accuracy achievable with this technique. From Table 3.2, the standard deviation in detonation velocity using the dynamically calibrated wavelength is 168 m/s. Density-correcting to 1.4 g/cm^3 reduces the standard deviation to 110 m/s. It should also be noted that the waveform data in the first shot was of poorer quality than the remaining shots. With the wavelengths shown in Table 3.2, the average percent difference between the dynamically calculated wavelength and the wavelength calculated with measured permittivity was less than 2%.

The experiments with HMX showed that it was possible to obtain detonation velocity

measurements with relatively low shot-to-shot standard deviations. Density adjustment to a powder density of 1.4 g/cm^3 could also be employed to yield additional improvements in detonation velocity. Also, good agreement between the dynamically calibrated wavelength and measurement-determined wavelength could be obtained, which was crucial for materials where available material was insufficient for measuring permittivity.

3.3   MDNT/CL-20 Detonation Experiment Results

Microscope images are shown for MDNT, the MDNT/CL-20 cocrystal, and CL-20 in Figs. 3.3 to 3.5. No morphological features could be discerned for the CL-20 particles due to their small size.

Four cocrystal samples were pressed to an average density of 1.398 $\pm$ 0.010 g/cm^3. Four physical mixture samples were pressed to an average density of 1.380 $\pm$ 0.026 g/cm^3. A measured permittivity was not available for either the cocrystal or MDNT. Therefore, the dynamic method was used to determine interference wavelength.

Using the process outlined for HMX, position-time plots were obtained from waveform data for the cocrystal and physical mix samples. Due to loss of data with one of the physical mix shots, data from only three shots is shown. The plots are shown in Figs. 3.6 to 3.7. As was the case with HMX, the plots show steady behavior from the start of the detonation event. The waviness in the position-time plot was due to transitions from one pressing increment to the next. Therefore, the entire event was treated as steady. The detonation velocity for the cocrystal was found to be 7.76 $\pm$ 0.113 km/s where $\pm$ 0.113 km/s represents the shot-to-shot variation in detonation velocity. The overall variation, i.e. combination of shot-to-shot standard deviation and measurement uncertainty, computed according to Eq. (3.16) is 156 m/s. The detonation velocity for the physical mixture was was measured to be 7.20 $\pm$0.050
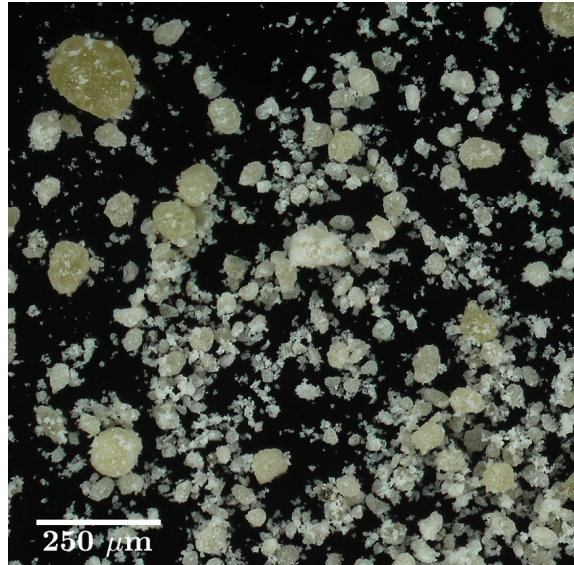
Figure 3.3. Microscope image of MDNT particles .
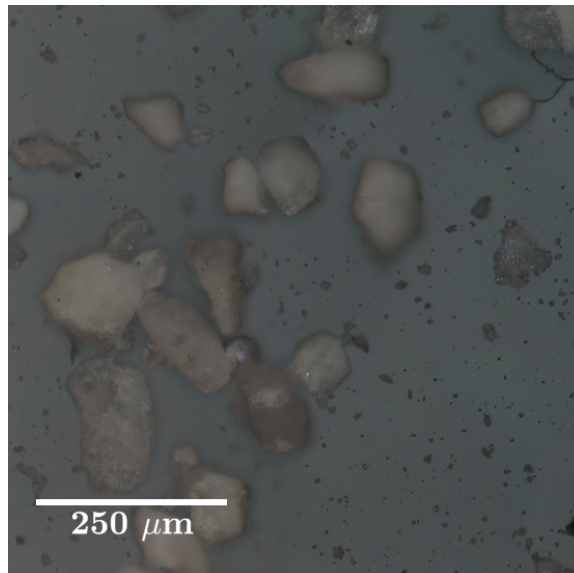
Figure 3.4. Microscope image of MDNT/CL-20 particles .

km/s. The overall variation, again using Eq. (3.16), for the physical mixture is 119 m/s.
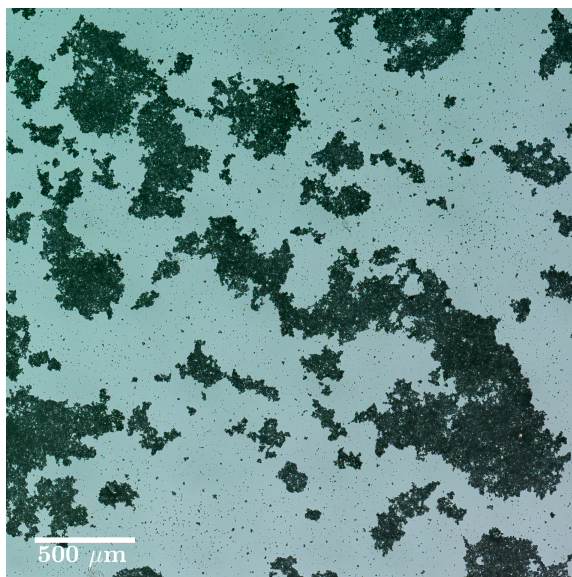
Figure 3.5. Microscope image of CL-20 particles .

The enthalpy of formation for the MDNT/CL-20 cocrystal was measured to be 1025 ± 147 kJ/mol. Using this number, the crystal density, and the chemical composition of the cocrystal, a reactant was created in CHEETAH. It was predicted in CHEETAH v7.0 that the cocrystal would detonate 230 m/s faster than the physical mixture. Similar to what was seen with HMX, a linear relationship was found between powder density and detonation velocity. Assuming that the measured detonation velocities would follow the same relationship, the density-adjusted detonation velocity for the cocrystal was computed to be 7.78 ± 0.113 km/s. Adjusting for density in this case had a negligible effect on the standard deviation. The overall variation in detonation velocity for the cocrystal after adjusting for density remained 156 m/s. Applying the same procedure to the physical mix measurements yielded a density-adjusted detonation velocity of $7.28 \pm .044$ km/s, with the overall variation being 116 m/s after incorporating measurement uncertainty.
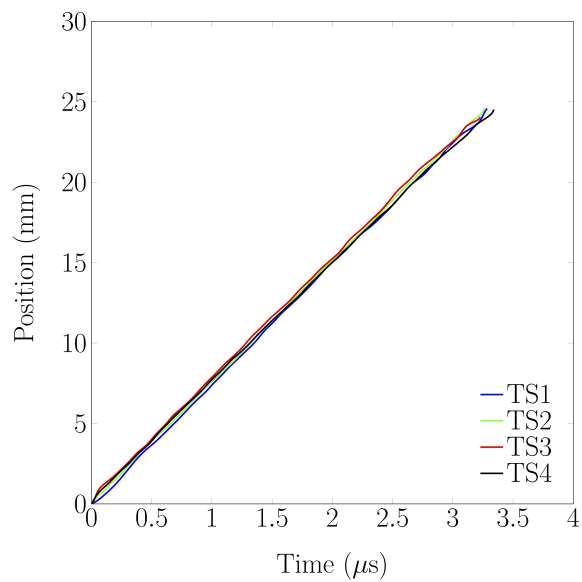
Figure 3.6. Position vs. time plots for MDNT/CL-20 Cocrystal detonation tests.
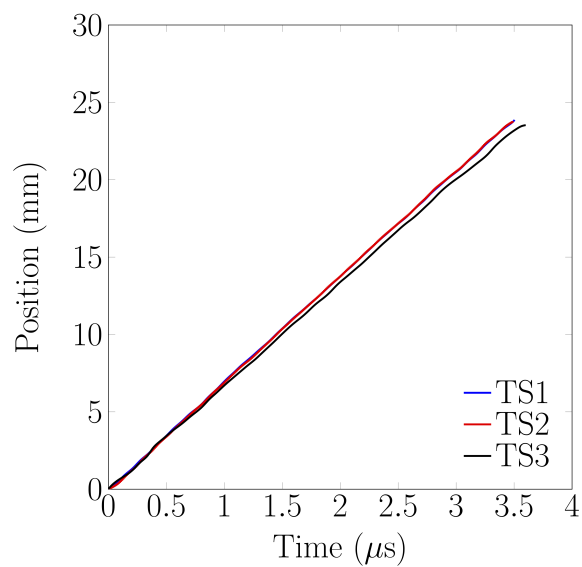
Figure 3.7. Position vs. time plots for MDNT/CL-20 Physical Mix detonation tests.

3.4 HMX/CL-20 Detonation Experiment Results

A microscope image of the HMX/CL-20 cocrystal particles is shown in Fig. 3.8. The characteristic plate-like structure of the HMX/CL-20 cocrystal can be seen in Fig. 3.8, similar to what Bolton *et al.* saw in their initial synthesis of this cocrystal [20].

A set of four cocrystal test samples were pressed to an average density of 1.437±0.027 g/cm^3. The physical mix test samples were pressed to a density of 1.438±0.032 g/cm^3. The permittivities of HMX and CL-20 are 3.5 and 3.3, respectively [84]. Using the Landau-Lifshitz mixing relation, the permittivity of the physical mixture at full density was calculated to be 3.4 [55,87]. The position-time plots for the HMX/CL-20 1:2 cocrystal and physical mixture are shown in Fig. 3.9 and Fig. 3.10, respectively.
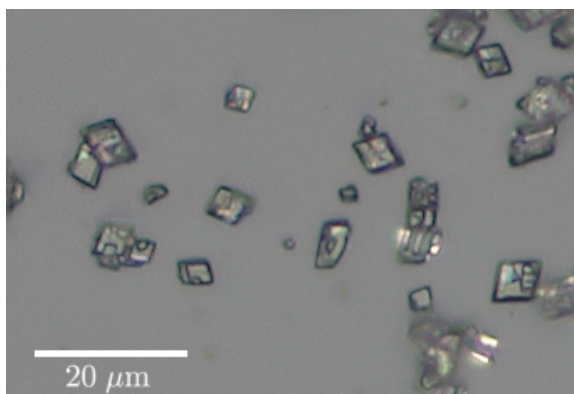
Figure 3.8. Microscope image of HMX/CL-20 particles.

The enthalpy of formation for the cocrystal was measured using bomb calorimetry. The molecular weight of the cocrystal was defined as $1M_{\text{CL-20}} + 0.5M_{\text{HMX}}$, where M denotes molecular weight in g/mol. This gives a molecular weight of 586.263 g/mol for the cocrystal. From bomb calorimetry tests, the enthalpy of formation for the HMX/CL-20 1:2 cocrystal was found to be 928 ± 130 kJ/mol. The enthalpy of formation for CL-20 is 377 kJ/mol and the enthalpy of formation for HMX is 75
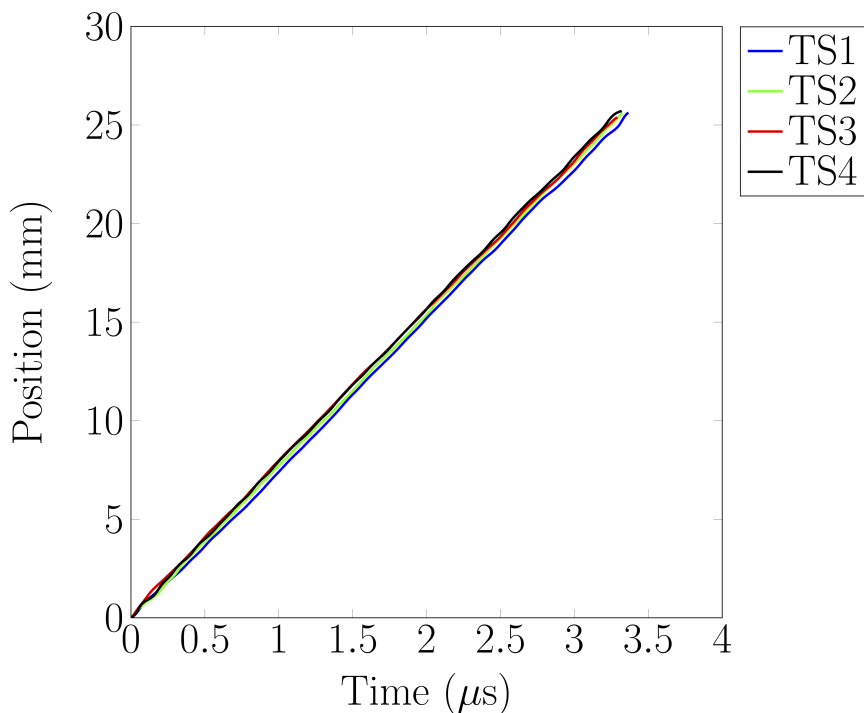
Figure 3.9. Position vs. time plots for HMX/CL-20 cocrystal detonation tests.

kJ/mol, which are found in [16] and [1], respectively. Using these numbers, the enthalpy of formation for the equivalent physical mixture is calculated to be 829 kJ/mol.

From Figs. 3.9 to 3.10, it can be seen that the assumption of prompt detonation could be used. Using the process outlined previously, the detonation velocity was computed and then adjusted to a charge density of 1.4 g/cm^3.

The density-adjusted detonation velocity computed using measured permittivity for the cocrystal was computed to be 7.57 ± 0.156 km/s. Using dynamically calculated wavelength, the density-adjusted detonation velocity for the cocrystal was found to be 7.54 ± 0.145 km/s.

The density-adjusted detonation velocity for the physical mixture using permittivity calculated using the Landau-Lifshitz mixing relation was found to be 7.24 ± 0.112
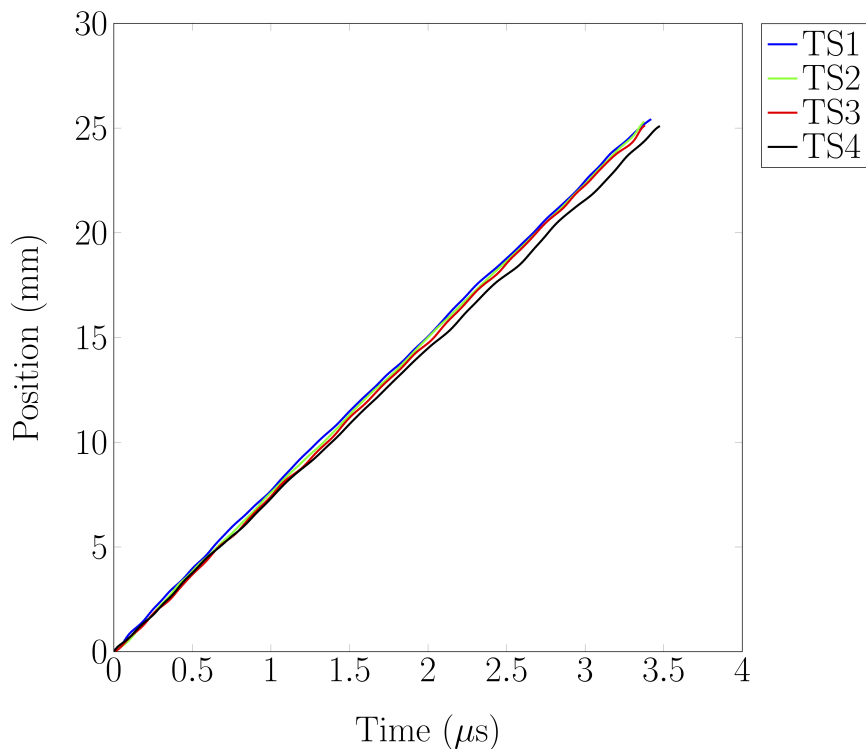
Figure 3.10. Position vs. time plots for HMX/CL-20 physical mix detonation tests.

km/s. The density-adjusted detonation velocity using dynamically calculated wavelength was found to be 7.30 ± 0.125 km/s.

It can be seen the range of detonation velocities for the HMX/CL-20 cocrystal and physical mixture appear to overlap, indicating that any observed difference is within the experimental uncertainty.

3.5 CL-20/HP Detonation Results

The CL-20/HP solvate particles are shown in Fig. 3.11. The particles exhibited a plate-like morphology. The material was visually distinguishable from CL-20.
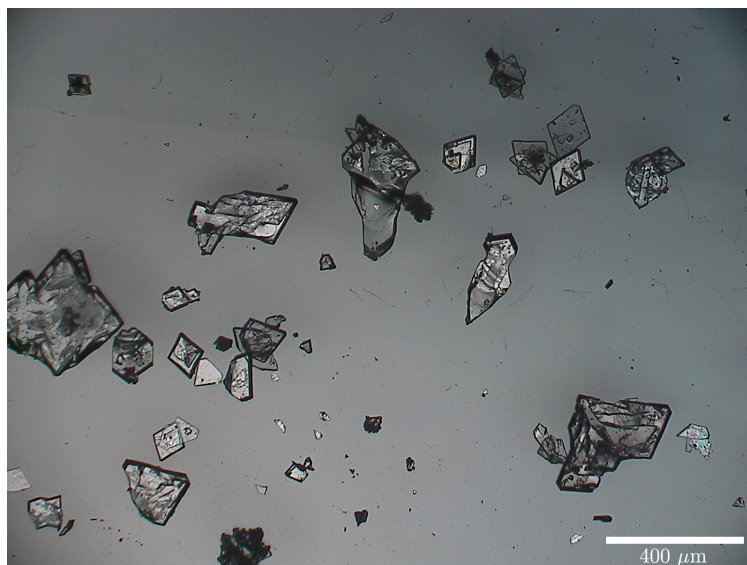
Figure 3.11. CL-20/HP solvate particles.

Five CL-20/HP test samples were pressed to an average density of 1.311 ± 0.084 g/cm^3. These charge densities were lower than the average densities obtained for other cocrystals presented so far, primarily due to loss of material during transfer from weigh dishes to pressing equipment. The measured detonation velocities for the CL-20/HP samples are shown in Fig. 3.12. These velocities are compared to CL-20. Four CL-20 samples were pressed to an average density of 1.327 ± 0.052 g/cm^3. The detonation velocity plots are shown in Fig. 3.13.
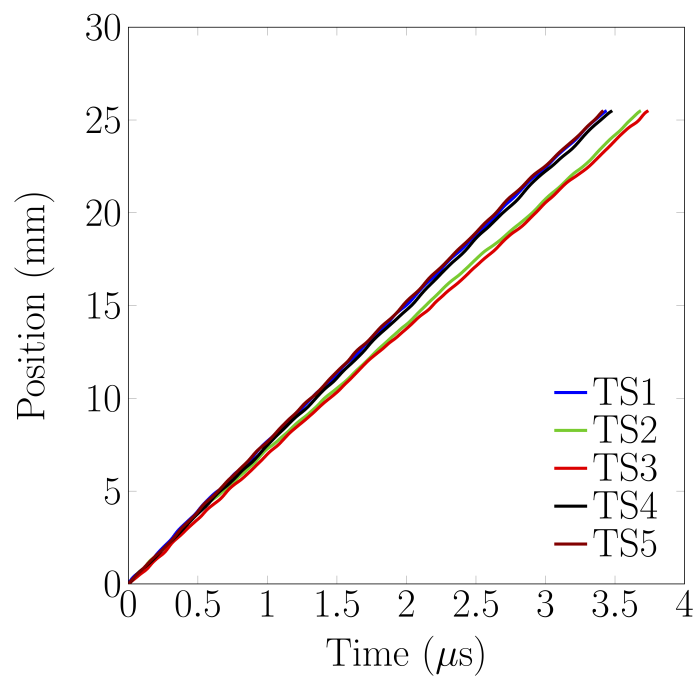
Figure 3.12. Position vs. time plots for CL-20/HP solvate detonation tests.
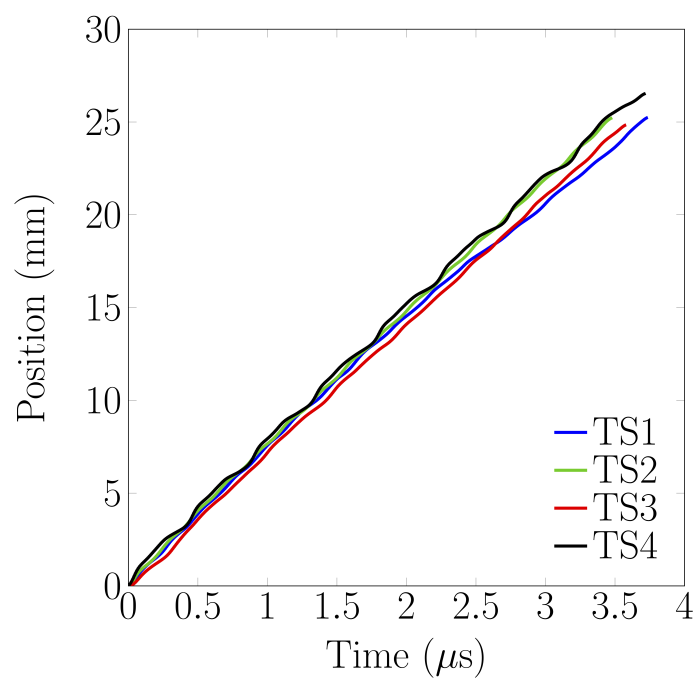
Figure 3.13. Position vs. time plots for CL-20 detonation tests.

The enthalpy of formation for the CL-20/HP solvate was measured to be 748 ± 128 kJ/mol. Using this value, along with measured crystal density and chemical formula, a new reactant was created in CHEETAH. The detonation velocities for the CL-20/HP solvate were also adjusted to a powder density of 1.4 g/cm³ using the process described previously. The same adjustment was done for CL-20. The density-adjusted detonation velocity for the CL-20/HP solvate was found to be 7.52 ± 0.133 km/s, which was about 3.2% higher than the predicted velocity of 7.28 km/s found in CHEETAH. The density-adjusted detonation velocity for CL-20 was found to be 7.22 ± 0.122 km/s, which was within about 0.3% of the predicted detonation velocity of 7.21 km/s found from CHEETAH.

3.6   ADNP/DAF Detonation Results

For the ADNP/DAF shots, PBX 9501 was used as the booster material. A new set of baseline experiments were performed with PBX 9501 as a booster and HMX as the sample material in order to determine the optimal loading density for the PBX 9501 so that it would promptly initiate the sample material to a detonation. PBX 9501 is 95% HMX with the remainder being binder. The PBX 9501 booster charge was pressed to 90% TMD. A sample interferometer waveform for the ADNP/DAF cocrystal is shown in Fig. 3.14. The time t = 0 in Fig. 2 corresponds to the burst current of the detonator being reached. The signal denoted by CH3 in Fig. 2 is the photodiode signal. The rise from the baseline in CH3 corresponds to detonator breakout. The fringes seen shortly after t = 0 in Fig. 2 were due to electromagnetic interference from the firing unit and detonator. The fringes seen between approximately 5 μs and 8 μs were due to sources of reflections present in the experimental setup prior to the detonation front arriving at the sample material. These fringes were observed for some test samples but were determined not to be characteristic of the booster charge detonation velocity.
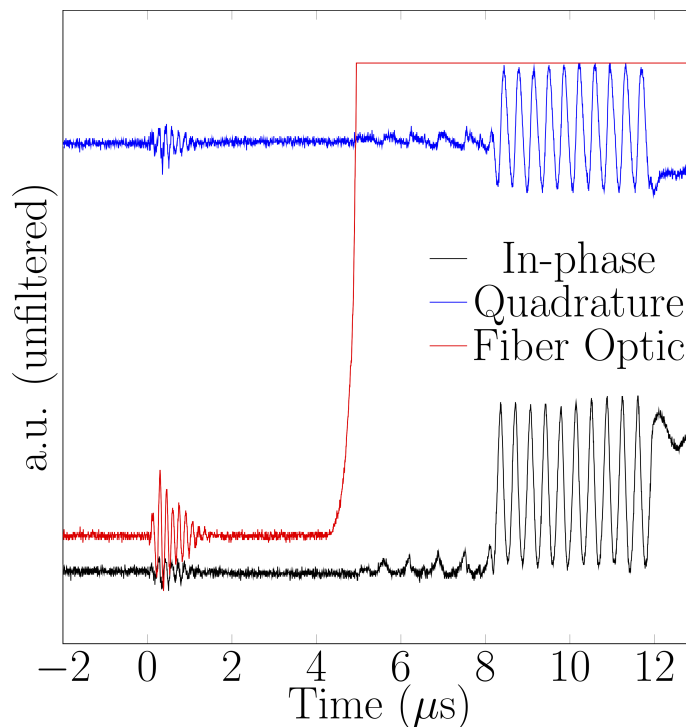
Figure 3.14. Sample MI data for MI experiments using linear current sensor.

The average loading density of three HMX detonation test samples was 1.429 ± 0.006 g/cm^3. Using the methods outlined in previous sections, position-time plots were obtained for three test samples and are shown in Fig. 3.15. It can be seen from Fig. 3.15 that little transient was present over the entire length of the sample charge, indicating that the booster charge was well-matched to the sample material.

Four ADNP/DAF cocrystal samples were pressed to an average density of 1.435 g/cm^3. The standard deviation was less than 0.001 g/cm^3. Four physical mix test samples were pressed to an average density of 1.438 ± 0.001 g/cm^3. Position vs. time plots for the cocrystal and physical mixture tests are shown in Figs. 3.16 to 3.17. The detonation velocity of the cocrystal from the four measurements was determined to be 6.72 ± 0.146 km/s. The detonation velocity of the physical mixture from the four measurements was determined to be 6.53 ± 0.142 km/s. The observed detonation velocities indicate that there may not be a significant difference between the
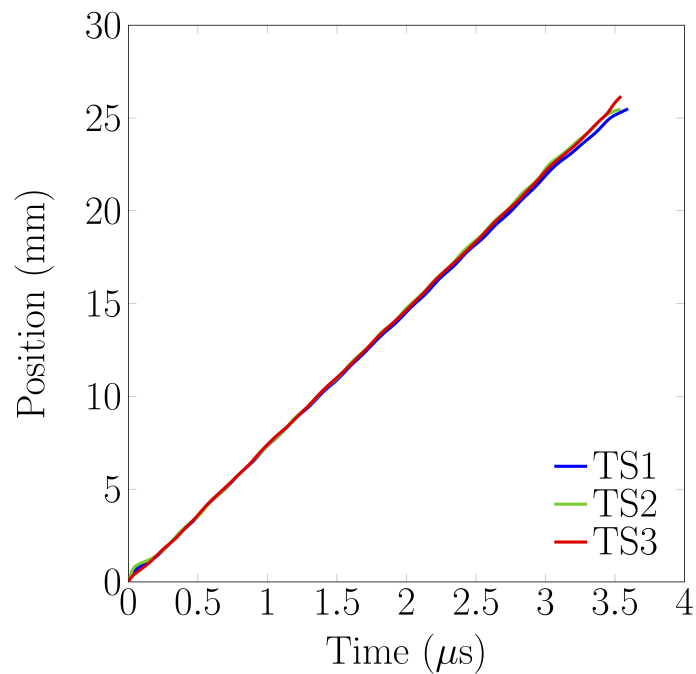
Figure 3.15. Position vs. time plots for HMX with PBX 9501 as booster.
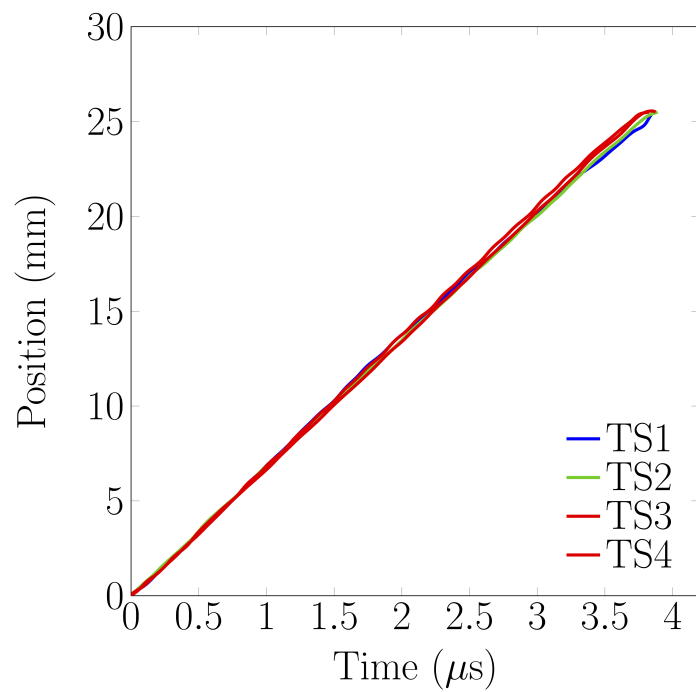
Figure 3.16. Position vs. time plots for ADNP/ DAF cocrystal.
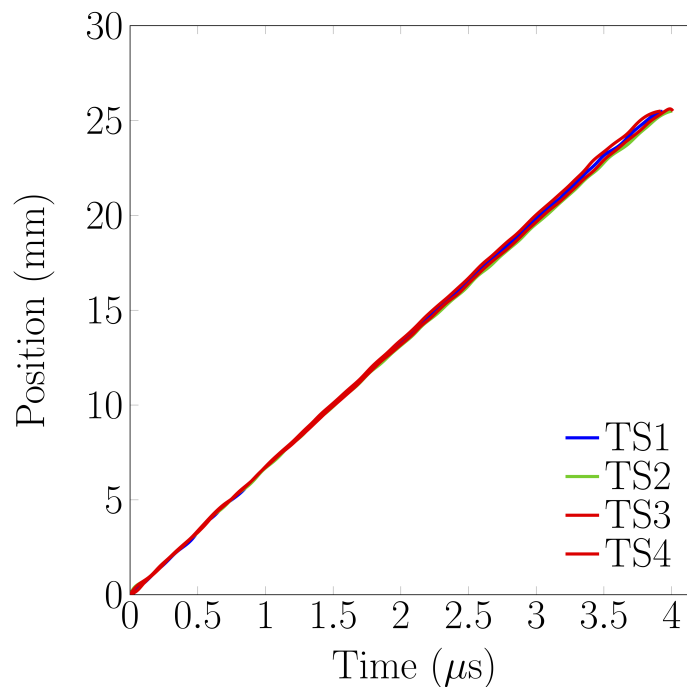
Figure 3.17. Position vs. time plots for ADNP/ DAF physical mixture.

ADNP/DAF cocrystal and formulation. This is partially attributable to phase purity of the cocrystal material used in detonation velocity measurements. However, a detonation experiment was performed with cocrystal prepared by Rosalyn Kent and Ren Wiscons at University of Michigan. The measured detonation velocity with this sample was measured to be 6.61 km/s. This is also within the range of the measured detonation velocities of the cocrystal.

A detonation shot was performed with DAF pressed to 1.4 g/cc. The filtered in-phase and quadrature channels with overlaid peaks are shown in Fig. 3.18.
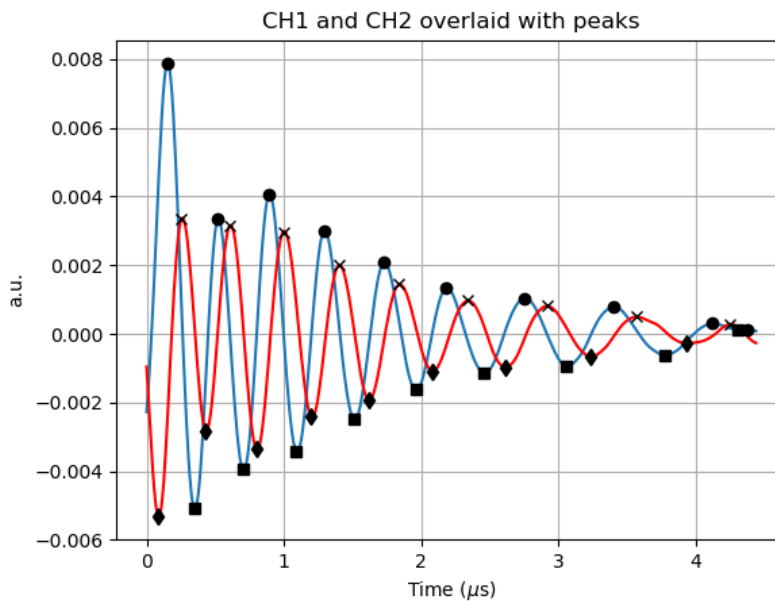
Figure 3.18. MI waveform for DAF detonation shot.

About 6.35 mm of the confiner was recovered after the shot. Additional shots were not performed since DAF failed to detonate at this diameter. This remaining amount was subtracted from the total charge length to compute the material wavelength according to Eq. (2.13). Using this wavelength, a position vs. time plot was constructed which is shown in Fig. 3.19. The decreasing frequency shown in Fig. 3.18 is indicative of detonation failure. This can also be seen in the position-time plot shown in Fig. 3.19. The DAF was not able to sustain a detonation. This indicates that DAF may not be detonable at this diameter.
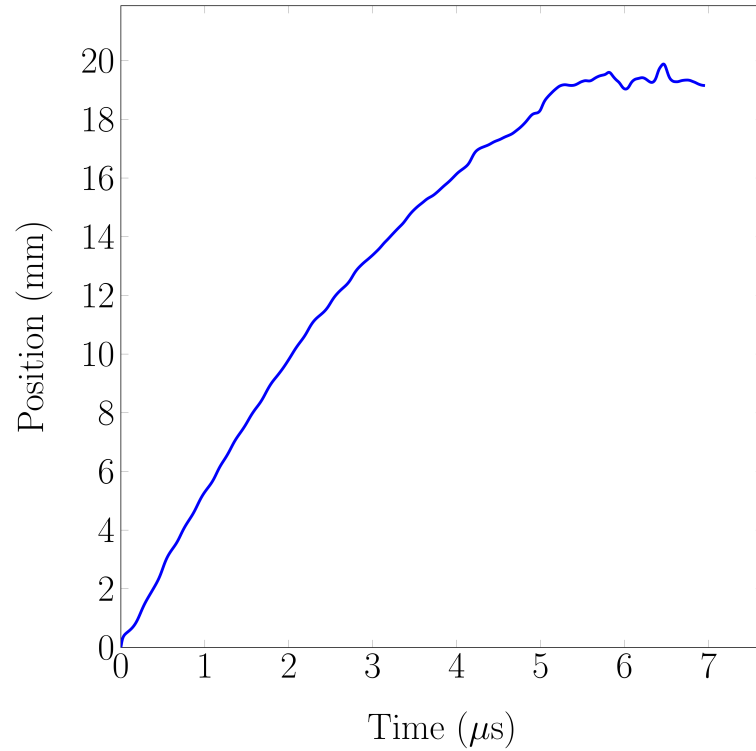
Figure 3.19. Position vs. time plot for DAF.

3.7 Discussion

3.7.1 Scale Analysis

It is well known that detonation velocity has a strong dependence on loading density. Kamlet *et al.* identified the moles of gas produced, average molecular weight of the gaseous products, and heat of detonation as additional factors that affect detonation velocity and pressure. A set of scaling relationships were identified using these factors [76]. The first equation is

$$\xi = NM^{1/2}Q^{1/2}, \tag{3.17}$$

where N is the number of moles of gas produced per gram of explosive, M is the average molecular weight of the gaseous products in g/mol, and Q is the heat of detonation in cal/g. The second equation is

$$P = K\xi\rho_0^2 = K\left(NM^{1/2}Q^{1/2}\right)\rho_0^2, \tag{3.18}$$

where ρ_0 is loading density P is detonation pressure and K is a constant. The Kamlet equation for detonation velocity is

$$D = A\xi^{1/2}\left(1 + B\rho_0\right) = A\left(NM^{1/2}Q^{1/2}\right)^{1/2}\left(1 + B\rho_0\right), \tag{3.19}$$

It can be seen from Eqs. (3.18) to (3.19) that loading density is the most dominant term. As mentioned previously, detonation velocities for all materials were compared at a fixed loading density. Taking the total differential of Eq. (3.17) and Eq. (3.19) and holding density constant, the resulting relation is

$$\frac{\Delta D}{D} = \frac{1}{2}\frac{\Delta\xi}{\xi}. \tag{3.20}$$

This states that if a difference in detonation speed between two explosives at an identical loading density is observed, the effect should show up in the remaining three factors that affect detonation velocity as shown in Eq. (3.17).

Expansion of the term $\Delta\xi$ yields

$$\mathrm{d}\xi = (MQ)^{1/2}\,\mathrm{d}N + \frac{1}{2}NM^{-1/2}Q^{1/2}\,\mathrm{d}M + \frac{1}{2}NM^{1/2}Q^{-1/2}. \tag{3.21}$$

Dividing both sides by ξ yields

$$\frac{\Delta\xi}{\xi} = \frac{\Delta N}{N} + \frac{1}{2}\frac{\mathrm{d}M}{M} + \frac{1}{2}\frac{\mathrm{d}Q}{Q} \tag{3.22}$$

Eq. (3.20) may be rewritten as

$$\frac{\Delta D}{D} = \frac{1}{2}\left[\frac{\Delta N}{N} + \frac{1}{2}\frac{\mathrm{d}M}{M} + \frac{1}{2}\frac{\mathrm{d}Q}{Q}\right] \tag{3.23}$$

Only thermodynamics were considered when determining the final products of the cocrystal and physical mixture. Since the same molecules are present in both the cocrystal and the physical mixture, the final products should be identical. Therefore, the scaling relationship described in Eq. (3.20) reduces to

$$\frac{\Delta D}{D} \sim \frac{1}{4}\frac{\mathrm{d}Q}{Q}, \tag{3.24}$$

which states that for identical moles of gas production, identical average molecular weight of the gaseous products, and identical loading density, the percentage change in detonation speed should be approximately equal to 25% of the percentage change in heat of detonation. This is consistent with the original Kamlet scaling relationships which show that density is the most dominant factor in both detonation velocity and pressure. The MDNT/CL-20 cocrystal was measured to detonate over 500 m/s faster than the physical mixture of the components when both were at the same density. This difference is greater than the measurement uncertainty. The enthalpy of formation of MDNT is 122 kJ/mol and the enthalpy of formation of CL-20 is 377 kJ/mol [16, 87]. The calculated enthalpy of formation of a physical mix of the components is therefore 499 kJ/mol. The measured enthalpy of formation of the cocrystal is 1025.19 kJ/mol. From Kamlet *et al.*, for loading densities greater than 1 g/cm^3, the products of chemical reaction of detonation may be assumed to be of the form

$$\mathrm{C}_a\mathrm{H}_b\mathrm{N}_c\mathrm{O}_d \rightarrow \left(\frac{1}{2}c\right)\mathrm{N}_2 + \left(\frac{1}{2}b\right)\mathrm{H}_2\mathrm{O} + \left(\frac{1}{2}d - \frac{1}{4}b\right)\mathrm{CO}_2 + \left(a - \frac{1}{2}d + \frac{1}{4}b\right)\mathrm{C} \tag{3.25}$$
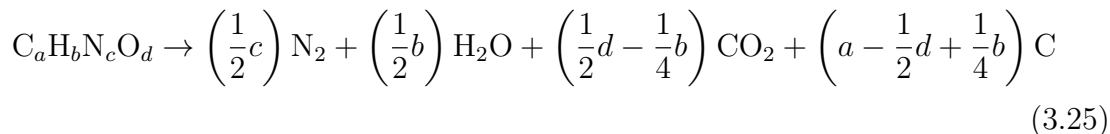
for a CHNO explosive. The heat of detonation is defined as

$$\bar{Q} = \sum \left(\Delta H_f^\circ\right)_{\text{products}} - \sum \left(\Delta H_f^\circ\right)_{\text{reactants}}, \tag{3.26}$$

where ΔH_f° is the enthalpy of formation. The products should be evaluated at the C-J state although this is not possible in practice. Experiments on detonation calorimetery with PETN showed that chemistry freeze occurs at approximately 1800 K [88].

Using enthalpy of formation data given in [89] for the assumed detonation products, the heats of detonation for the MDNT/CL-20 cocrystal and physical mixture were calculated to be 7.16 kJ/g and 6.3 kJ/g, respectively. Using Eq. (3.24), the percentage difference in detonation speed between the cocrystal and physical mixture should be 3.4%. This means that the cocrystal should detonate 300 m/s faster than the physical mixture based on an average velocity of 7.5 km/s. However, the cocrystal was observed to detonate 500 m/s faster or 8.6% faster than the physical mixture. The measurement uncertainty in the detonation speed is 1.51%. The error in the enthalpy of formation is about 14%. Taking this standard deviation in enthalpy of formation into account, the cocrystal could still be predicted to detonate approximately 4% or 300 m/s faster than the physical mixture.

Applying a similar analysis to the HMX/CL-20 cocrystal, the difference in heat of detonation on a per-gram basis is only 2.4%. Using the assumption of reaction products and the Kamlet equations, the detonation velocity of the cocrystal was calculated to be 7.43 km/s, which is within the experimental error of the measured detonation velocity. Since the heats of detonation between the HMX/CL-20 cocrystal and mixture are so similar, the difference in detonation velocity is not measurable.

As a first step, a sensitivity analysis was performed to examine the effect of being slightly off of the expected 2:1 molar ratio of CL-20 and HMX in the physical mixture. It was determined from this analysis that even if the mixture was 50% excess HMX, i.e. a 1:1 molar ratio of HMX to CL-20 rather than 2:1, the physical mix would still detonate less than 100 m/s slower than the cocrystal. The shot-to-shot variations were also relatively small, indicating that the HMX and CL-20 were sufficiently well-mixed.

The intervals of detonation velocities based on the overall standard deviation for the HMX/CL-20 cocrystal and physical mixture overlap, indicating that there is no

measurable difference with the technique used. Even if an observable difference could be detected with a more precise measurement technique, this difference would likely not be attributable to thermodynamics.

The CL-20/HP solvate has a higher enthalpy of formation than that of CL-20. Using the predicted product species for each material obtained from Eq. (3.25), the heat of detonation computed with Eq. (3.26) is 6.79 kJ/g for the CL-20/HP solvate and 6.56 kJ/g for CL-20. Using Eq. (3.19), the detonation velocity of the solvate 7.38 km/s and the detonation velocity for CL-20 is 7.24 km/s, both at 1.4 g/cm^3. The solvate was observed to detonate about 300 m/s faster than CL-20. The improved oxygen balance and higher enthalpy of formation of the solvate appears to account for half of the observed difference in detonation velocity. The calculated enthalpy of formation for a formulation of CL-20 and HP in the molar ratio seen in the solvate is 561 kJ/mol. This is about 25% lower than the measured enthalpy of formation of the solvate although the observed standard deviation for enthalpy of formation was 18%. Using this enthalpy of formation, the predicted detonation velocity of a physical mixture of CL-20 and HP is 7.37 km/s, which is indistinguishable from the calculated velocity of the solvate using the Kamlet relations. Bennion *et al.* claimed that the orthorhombic CL-20/HP solvate would detonate faster than ϵ-CL-20 using predictions in CHEETAH v7.0 and JCZ EOS. Using the measured enthalpy of formation, the Kamlet equations affirm this result. Using the Kamlet equations, the orthorhombic CL-20/HP solvate is predicted to detonate about 150 m/s faster than ϵ-CL-20.

The difference in detonation velocity between the ADNP/DAF cocrystal and physical mixture was within the expected experimental uncertainty. In addition, DAF failed to detonate at a loading density of 1.4 g/cm^3. The chemical formula for DAF is $C_2H_4N_4O$. Therefore, the oxygen balance is -79%, indicating limited gas production. Although DAF was detonated at a relatively small charge diameter, DAF may not be detonable since it is relatively under-oxidized.

The combined chemical formula of ADNP/DAF is $C_5H_7N_9O_5$, giving it an oxygen balance of about -50%, while the oxygen balance for ADNP is -32%. Using the predicted products species as described, the average molecular weight of the gaseous products from detonation of the cocrystal is slightly lower than it is for ADNP alone. However, the presence of DAF in the cocrystal system increases the total moles of gas produced. However, lack of enthalpy of formation data precludes further analysis based on the Kamlet scaling relations.

The above analysis establishes that the observed difference in detonation velocity between cocrystals and their corresponding physical mixtures for an identical loading density is due to differences in enthalpy of formation. The important question is therefore the reason for differences in enthalpy of formation between a cocrystal and its corresponding physical mixture.

Hess's law for heat summation states that total enthalpy of a chemical reaction is the same regardless of the steps taken to go from initial state to final state. Using this summation rule, the enthalpy of formation in the condensed phase can be considered the difference between enthalpy of formation in the gas phase and the enthalpy of sublimation [90]. The equation for condensed phase enthalpy of formation is

$$\Delta H^{\circ}_{f,c} = \Delta H^{\circ}_{f,g} - \Delta H_{sub}, \tag{3.27}$$

where $\Delta H^{\circ}_{f,c}$ is condensed phase enthalpy of formation, $\Delta H^{\circ}_{f,g}$ is gas-phase enthalpy of formation and ΔH_{sub} is the enthalpy of sublimation. The enthalpy of sublimation is related to the lattice energy of the crystalline material [91].

It is known that polymorphs can have differing enthalpies of formation. CL-20 for example, has a number of polymorphs in which the orientation of its nitro groups is changed [92]. For example, the enthalpy of formation for ϵ-CL-20 is 377 kJ/mol and the enthalpy of formation for $\beta-$CL-20 is 431 kJ/mol, a difference of 14%. However,

the effect of this difference in enthalpy of formation on detonation velocity when comparing at the same loading density is insignificant. This prediction is consistent with the idea that the difference in energies between various CL-20 conformer energies is small.

It should be noted that a computational study was performed by Duan *et al.* on a set of CL-20 cocrystals, including the MDNT/CL-20 cocrystal. The heat of formation was calculated according to Eq. (3.27) using isodesmic reactions [93]. The gas-phase ΔH_f° was found to be 726.5 kJ/mol [93]. In a separate study, Ma *et al.* reported the formation of a cocrystal of CL-20 and 1-methyl-3,4,5-trinitropyrazole (MTNP). The ΔH_f° for the individual components and the cocrystal were calculated using the ab initio method. The calculated ΔH_f° of the cocrystal was computed to be more than double that of a formulation of the compounds [94]. It is not clear in these two cases how energy is stored in these molecules since bond energies of intermolecular interactions are quite small compared to chemical bonds within molecules.

3.7.2 Statistical Analysis

The question of whether the observed differences between cocrystals and physical mixtures is significant may also be analyzed using statistical analysis and hypothesis testing. The null and alternative hypotheses are

$$H_0: \mu_{\text{CC}} = \mu_{\text{PM}} \tag{3.28}$$

and

$$H_a: \mu_{\text{CC}} \neq \mu_{\text{PM}}, \tag{3.29}$$

where μ_{CC} and μ_{PM} represent the mean detonation velocities of the cocrystal and physical mixture, respectively.

A critical assumption is whether the observed detonation velocity, the random variable in question, can be assumed to follow a normal distribution. It may be reasonably assumed that a large of number of test samples prepared to high precision, i.e. no significant variation in pressing density between samples, there is likely to be little shot-to-shot variation in observed detonation speed. If overall variance in detonation speed is defined according to Eq. (3.16) as the sum of the square of the shot-to-shot variance and measurement uncertainty, the overall variance converges could be expected to converge to measurement uncertainty with a large sample size. This variance would be finite and non-zero. Under the central limit theorem, the distribution of observed detonation speed would converge to a normal distribution in the limit of a large sample size [95]. Given the small sample size, the Student's t-distribution is appropriate. In addition, it was shown that we may reasonably assume the underlying distribution is Gaussian.

With population variances unknown and assumed to be unequal, the value of the t-statistic is

$$t_s = \frac{\bar{D}_{\mathrm{CC}} - \bar{D}_{\mathrm{PM}}}{s_p\sqrt{\frac{1}{n_{\mathrm{CC}}} + \frac{1}{n_{\mathrm{PM}}}}}, \tag{3.30}$$

where n_{CC} and n_{PM} are the numbers of cocrystal and physical mixture test samples, respectively. The terms $\bar{D}_{\mathrm{CC}}$ and $\bar{D}_{\mathrm{PM}}$ represent the observed average detonation speeds for the cocrystal and physical mixture, respectively. Similarly, n denotes the respective sample sizes. The term s_p is the paired standard deviation, defined as [96]:

$$s_p^2 = \frac{(n_{\mathrm{CC}} - 1)s_{\mathrm{CC}}^2 + (n_{\mathrm{PM}} - 1)s_{\mathrm{PM}}^2}{n_{\mathrm{CC}} + n_{\mathrm{PM}} - 2}, \tag{3.31}$$

where s denotes the sample standard deviation and the subscripts CC and PM denote cocrystal and physical mixture, respectively.

For the measured HMX detonation velocities, we may construct a 95% confidence interval (CI). The 95% CI is $\left[\bar{D} - t_{\alpha/2,n-1}\frac{s}{\sqrt{n}}, \bar{D} + t_{\alpha/2,n-1}\frac{s}{\sqrt{n}}\right]$, where α is the desired level of significance and n is the number of test samples [95]. As described previously, the overall standard deviation with HMX was 109 km/s at a powder density of 1.4 g/cm^3. Therefore, a 95% CI for the detonation speed for HMX obtained with experiment described previously is $[7.01, 7.27]$ km/s. In Hobbs *et al.* , two measurements for HMX at the same powder density in a 25 mm diameter charge were reported to be 7.2 and 7.3 km/s [24]. One of the measurements is within the CI and the other measurement is slightly outside the CI. Therefore, the detonation velocities for HMX obtained in this work at a charge diameter of 6.52 mm and powder density of 1.4 g/cm^3 are comparable to measurements at larger scales.

The measured detonation velocities for the MDNT/CL-20 cocrystal and physical mixture were found to be 7.72 ± 0.156 km/s and 7.20 ± 0.113 km/s, respectively. Using Eqs. (3.30) to (3.31), the value of the t-statistic is 5.11. Using the SciPy package [97], the critical value of t, denoted by t_c was computed to be 2.015. A plot of the Student's t distribution probability density function (PDF) is shown in Fig. 3.20. In between blue regions shown in Fig. 3.20, the null hypothesis holds true.

Since the alternative hypothesis is $\mu_{\text{CC}} \neq \mu_{\text{PM}}$, it is necessary to calculate both $P(t \leq t_s)$ and $P(t \geq t_s)$, where t_s is the value of t calculated in Eq. (3.30). This is equivalent to calculating $2P(t \geq 4.85)$, which is also called the p-value. The p-value is calculated as

$$p = 2(1 - \text{CDF}(t)), \tag{3.32}$$

where $\text{CDF}(t)$ is the cumulative distribution function (CDF).
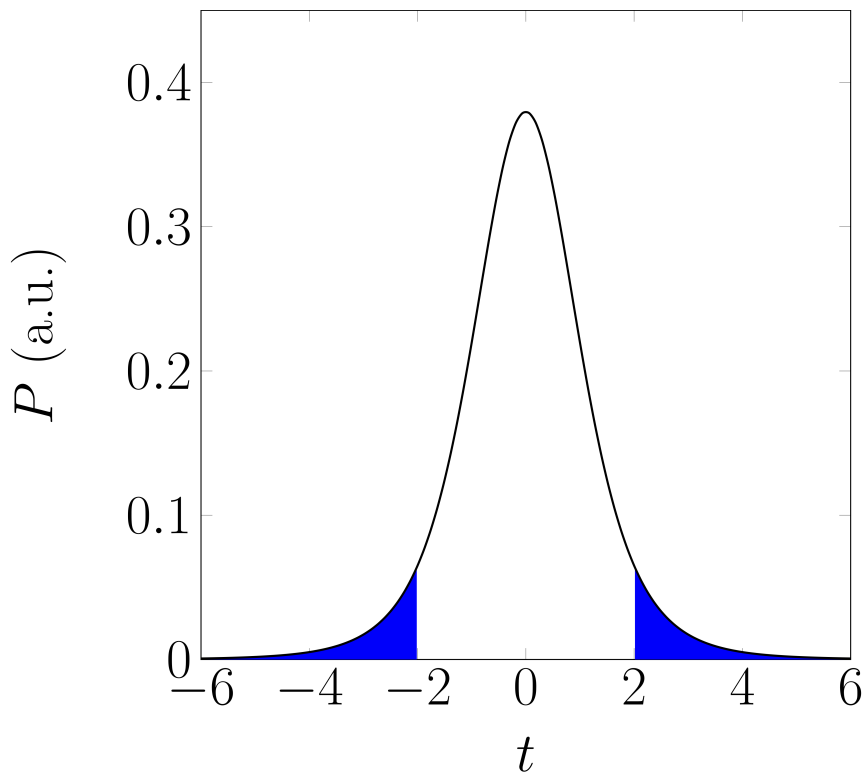
Figure 3.20. Student's t distribution PDF showin critical regions.

Using the SciPy package [97], the p-value for the hypothesis test applied to the MDNT/CL-20 data was calculated using Eq. (3.32) to be 3.7×10^{-3} or 0.37%. Common values of α, known as levels of significance, include 0.1, 0.05, and 0.01 (or 10%, 5%, and 1%). The level of significance indicates the probability of incorrectly rejecting the null hypothesis. In the context of this work, the value of α is the probability of incorrectly inferring that a difference exists between a cocrystal and its physical mixture. Even for a significance level of 0.01, the the p-value is still below the level of significance. There is a relatively low probability of incorrectly rejecting the null hypothesis when it is true.

The probability of a hypothesis test yielding a false positive, denoted by β is another important parameter. A false positive occurs when the null hypothesis is false but the hypothesis test fails to reject it. A failure to reject the null hypothesis would occur

when the computed value of the t-statistic is less than the critical value. The critical value of t, denoted by t_c is found based on degrees of freedom, $\nu = n_{CC} + n_{PM} - 2$, and the chosen value of α. Starting with Eq. (3.30), the left-hand side is set equal to t_c, i.e. $t = t_c$ and solved for $\bar{D}'_{CC}$. With MDNT/CL-20 for example, using a significance level of 0.05, $t_c = 2.015$ so the value of D'_{CC} is 7.405 km/s.

Using the value of $\bar{D}'_{CC}$, one obtains a new value of the t-statistic, denoted by t', which is obtained by computing

$$t' = \frac{\bar{D}'_{CC} - \bar{D}_{CC}}{s_p \sqrt{\frac{1}{n_{CC}} + \frac{1}{n_{CC}}}}, \tag{3.33}$$

where $\bar{D}_{CC}$ is the average detonation speed for the cocrystal. Using the computed value of t', the value of β is obtained by calculating $P(t \leq t')$. The quantity $P(t \leq t')$ is the value of the CDF of the t-distribution.

The value of α affects the value of t_c, the critical value of the t-statistic. Thus, the value of the β and consequently the power of the hypothesis test is dependent on the chosen significance level. In the context of this work, the value of β is the probability that the test infers no significant difference exists between a cocrystal and its formulation, i.e. fails to reject the null hypothesis. As the complement of β, the power of the hypothesis test is the probability of correctly rejecting the null hypothesis. The calculated p-values and powers based on various levels of significance are shown in Table 3.3. In Table 3.3, the row HMX/CL-20 (m) and HMX/CL-20 (d) denote respectively the detonation speeds obtained using directly measured and dynamically calculated material wavelengths.

As mentioned elsewhere, the MDNT/CL-20 cocrystal was observed to detonate measurably faster than its physical mixture. The Kamlet scaling laws demonstrated that the difference in enthalpy of formation between the cocrystal and physical mixture partially accounts for the observed difference. The p-value for the MDNT/CL-20

Table 3.3. Calculated p-values and powers.

		Power		
	p	$\alpha = 5\%$	$\alpha = 2\%$	$\alpha = 1\%$
MDNT/CL-20	0.373%	98.8%	97.0%	93.3%
HMX/CL-20 (m)	1.39%	90.7%	77.9%	61.1%
HMX/CL-20 (d)	4.61%	70.3%	46.0%	27.4%
CL-20/HP	0.711%	95.4%	88.3%	77.4%
ADNP/DAF	11.1%	47.0%	24.2%	12.4%

data is smaller than even a 1% level of significance, meaning it is relatively unlikely that the result is statistically significant even with such a stringent threshold. The results from statistical analysis appear to be in agreement with the predictions of theory.

The HMX/CL-20 statistical results are not as definitive, however. The data obtained with measured permittivity display statistical significance for a 2% threshold as evidenced by the p-value of 1.38%. However, the data with dynamically calculated wavelength would only be statistically significant for a 5% threshold. This result is in agreement with the theory, which shows that the difference in detonation speed would be quite small for the HMX/CL-20 cocrystal and physical mixture at the same loading density due to insignificant differences in enthalpy of formation. The theory is also in agreement with statistical analysis for the CL-20/HP solvate. Due to lack of enthalpy of formation data for the ADNP/DAF cocrystal, the difference in detonation speed between the cocrystal and its physical mixture cannot be predicted from theory. The results of statistical analysis do not appear to show significance. However, the power of the hypothesis test for ADNP/DAF is lower, meaning that there is a relatively high probability of a false positive for this material. This could be improved with additional samples. In addition, we note that if the same standard deviations for the ADNP/DAF cocrystal and physical mixture were observed for eight samples of each

instead of only four, the p-value would be 1.38% which would statistically significant for a chosen α value as small as 2%.

4. CONCLUSIONS

In this work, small-scale experiments were performed to obtain comparative detonation velocity measurements of cocrystals and their corresponding physical mixtures. Using as little as 1.2 g of material per test, it was demonstrated that well-resolved measurements of detonation velocity with variations on the order of 130 m/s could be obtained. A critical element of this was control of loading density to minimize shot-to-shot variation. In addition, it was shown that the booster material could be well-matched to the sample material. The C-J pressure of the booster charge was well above the C-J pressure of the sample material. As a result, the length of transient shock propagation in the sample material was negligible. Therefore, it could be accurately assumed that the sample material was promptly initiated to a detonation. A major benefit of this assumption was that materials for which permittivity data were not available, material wavelength could be calculated dynamically. Obtaining interference wavelength in this manner was useful for materials available in limited supply.

The two categories of experimental error are random error and bias error. It was demonstrated in this work that random error can be minimized to yield repeatable shots. Since explosives used in this work were ideal explosives with small critical diameter, it is unlikely the scale had a significant effect on the results. Another potential source of bias error is due to interaction of the reaction zone with the confiner which affects detonation velocity. However, a feature of ideal explosives is a thin reaction zone. The thickness of the confiner is 700 μm, which is likely much thicker than the width of the reaction zone. Furthermore, the confinement was identical in all cases. Therefore, it is unlikely that confiner interactions are a source of bias error.

For the explosives used in this work, a purely thermodynamic treatment was applied.

It was demonstrated above that it can be reasonably assumed that the detonation is within the regime of thermodynamics. Since small-scale detonation testing is intended to provide information about integrated without the requirement for large amounts of material, it can be concluded that small-scale testing is most appropriate when the detonation is within the regime of thermodynamics, which is independent of scale. Achieving these conditions is dependent on the material. The small-scale experiment used in this work is appropriate for ideal explosives with critical diameters well below the experimental charge diameter of 6.52 mm.

A significant focus of this work was on CL-20 cocrystals due to availability. It was found that the MDNT/CL-20 cocrystal detonates 500 m/s faster than the physical mixture. Based on analysis of scaling relationships from the Kamlet equations, this difference should be attributable to the large difference in enthalpy of formation between the cocrystal and physical mixture. If enthalpy of formation is different between the cocrystal and physical mixture, there would be a difference observed between the cocrystal and physical mixture if the two are at the same density. The enthalpy of formation of the MDNT/CL-20 cocrystal was double that of the physical mixture. The reason for such a large enthalpy of formation difference remains an open question. By contrast, the HMX/CL-20 cocrystal enthalpy of formation was within the measurement uncertainty of the measurement. Therefore, for the HMX/CL-20 cocrystal and physical mixture at the same loading density, the detonation velocities should not differ significantly. The observed difference was within measurement uncertainty. The CL-20/HP solvate was found to detonate faster than CL-20. This result is attributable to the large difference in enthalpy of formation of the solvate and CL-20. The enthalpy of formation of a formulation of hydrogen peroxide and CL-20 in in a 1:2 molar ratio is within the measurement uncertainty of the measured enthalpy of formation of the physical mixture, which affirms that differences in detonation velocity are due to the enthalpy of formation, which alters the heat release from detonation.

These results imply that if density is held constant, thermodynamic detonation parameters, i.e. detonation pressure and velocity are attributable to differences in enthalpy of formation. It should be noted though that other aspects of detonation performance such as corner turning and shock initiation do not fall under a thermodynamic treatment of detonation. As noted previously, while discovery of cocrystals is less involved than discovery of novel energetic molecules, the former is by no means trivial. Therefore, it is useful to know beforehand whether the performance improvements obtained, if any, justify the investment of resources into discovery of a particular cocrystal. Computational efforts in predictions of crystal structure may be directed towards cocrystals that yield improvements in enthalpy of formation. However, cocrystals are complex molecules. Therefore, this remains an ongoing effort due to the expensive computational resources required for analyzing such complex molecules.

Similar to the goal of pharmaceutical cocrystal formation, the goal of energetic cocrystal formation is to obtain new materials that have improved properties in a shorter time-frame than it would take with the conventional route of new molecule discovery. Ideally, the cocrystal would exhibit synergistic interactions. For example, the TNT/CL-20 and HMX/CL-20 cocrystals both exhibited improved impact sensitivity relative to that of CL-20. In both cases, the impact sensitivities were similar to those of the less sensitive component. In addition, the ADNP/DAF cocrystal exhibits the property of having a stable melt phase, something ADNP does not. However, the improvements realized thus far are not relevant to thermodynamic effects. It is only in the case of the CL-20/HP solvate that thermodynamics can explain a slightly higher predicted detonation velocity than that of CL-20. However, even in the case of the solvate, it is expected to be similar to a formulation of the components. Therefore, from a purely thermodynamic standpoint, cocrystals are likely to be similar to a formulation of the components. Another point to note is that no cocrystal reported

thus far or analyzed in this work is predicted to detonate faster than CL-20. This is attributable to the unavoidable reduction in density that results from forming a cocrystal of CL-20 with a low-density coformer. The only exception is the CL-20/HP solvate. This difference is attributable to the improvement in oxygen balance. In addition to an improved oxygen balance, the orthorhombic CL-20/HP solvate has a density comparable to that of $\epsilon-$CL-20. The original goal of energetic cocrystallization was to use existing molecules that failed to achieve widespread production to form cocrystals that may overcome the reasons that lead to the failure of that particular molecule. While CL-20's conformational diversity makes it attractive as a coformer for energetic cocrystals, cocrytallization of CL-20 results in the loss of CL-20's most attractive feature-its high density and consequently superior detonation performance. Therefore, discovery efforts in energetic cocrystals may be more productively directed towards other molecules.

REFERENCES

REFERENCES

[1] Paul W. Cooper. *Explosives Engineering*. Wiley-CVCH, 1996.

[2] Noboru Ono. *The Nitro Group in Organic Synthesis*. Wiley Series in Organic Nitro Chemistry. John Wiley & Sons, Inc., New York, USA, apr 2001.

[3] Gautam R. Desiraju. Supramolecular Synthons in Crystal EngineeringA New Organic Synthesis, nov 1995.

[4] Linus Pauling. *The nature of the chemical bond and the structure of molecules and crystals : an introduction to modern structural chemistry*. Cornell University Press, 1960.

[5] Sławomir Grabowski. *Analysis of Hydrogen Bonds in Crystals*, volume 6. 2016.

[6] A I. Kitaigorodsky. *Mixed Crystals*, volume 33 of *Springer Series in Solid-State Sciences*. Springer Berlin Heidelberg, Berlin, Heidelberg, 1984.

[7] Örn Almarsson and Michael J. Zaworotko. Crystal engineering of the composition of pharmaceutical phases. Do pharmaceutical co-crystals represent a new path to improved medicines? *Chemical Communications*, 0(17):1889–1896, aug 2004.

[8] Ning Shan and Michael J. Zaworotko. The role of cocrystals in pharmaceutical science. *Drug Discovery Today*, 13(9-10):440–446, may 2008.

[9] David IA Millar, William G Marshall, Iain DH Oswald, and Colin R Pulham. High-pressure structural studies of energetic materials. *Crystallography Reviews*, 16(2):115–132, 2010.

[10] Tomislav Friščić and William Jones. Benefits of cocrystallisation in pharmaceutical materials science: An update. *Journal of Pharmacy and Pharmacology*, 62(11):1547–1559, 2010.

[11] Wildon Fickett and William C. Davis. *Detonation Theory and Experiment*. Dover Publications, Inc., 1979.

[12] Raymond S. George, Howard H. Cady, Raymond N. Rogers, and Robert K. Rohwer. Solvates of octahydro-1,3,5,7- tetranitro- 1,3,5,7- tetrazocine (HMX): Relatively Stable Monosolvates. *Industrial and Engineering Chemistry Product Research and Development*, 4(3):209–214, sep 1965.

[13] RE Cobbledick and RWH Small. The crystal structure of the δ-form of 1, 3, 5, 7-tetranitro-1, 3, 5, 7-tetraazacyclooctane (δ-hmx). *Acta Crystallographica Section B: Structural Crystallography and Crystal Chemistry*, 30(8):1918–1922, 1974.

[14] Kira B. Landenberger and Adam J. Matzger. Cocrystal engineering of a proto-type energetic material: Supramolecular chemistry of 2,4,6-trinitrotoluene. *Crystal Growth and Design*, 10(12):5341–5347, 2010.

[15] Kira B. Landenberger and Adam J. Matzger. Cocrystals of 1,3,5,7-Tetranitro-1,3,5,7-tetrazacyclooctane (HMX). *Crystal Growth & Design*, 12(7):3603–3609, jul 2012.

[16] R. L. Simpson, P. A. Urtiew, D. L. Ornellas, G. L. Moody, K. J. Scribner, and D. M. Hoffman. CL-20 performance exceeds that of HMX and its sensitivity is moderate. *Propellants, Explosives, Pyrotechnics*, 22(5):249–255, 1997.

[17] Arnold T. Nielsen, Andrew P. Chafin, Stephen L. Christian, Donald W. Moore, Melvin P. Nadler, Robin A. Nissan, David J. Vanderah, Richard D. Gilardi, Clifford F. George, and Judith L. Flippen-Anderson. Synthesis of polyazapolycyclic caged polynitramines. *Tetrahedron*, 54(39):11793 – 11812, 1998.

[18] Jessica H Urbelis and Jennifer A Swift. Solvent effects on the growth morphology and phase purity of CL-20. *Crystal Growth and Design*, 14(4):1642–1649, 2014.

[19] Onas Bolton and Adam J. Matzger. Improved stability and smart-material functionality realized in an energetic cocrystal. *Angewandte Chemie International Edition*, 50(38):8960–8963, 2011.

[20] Onas Bolton, Leah R. Simke, Philip F. Pagoria, and Adam J. Matzger. High power explosive with good sensitivity: A 2:1 cocrystal of CL-20:HMX. *Crystal Growth and Design*, 12(9):4311–4314, 2012.

[21] Zongwei Yang, Hongzhen Li, Hui Huang, Xiaoqing Zhou, Jinshan Li, and Fude Nie. Preparation and Performance of a HNIW/TNT Cocrystal Explosive. *Propellants, Explosives, Pyrotechnics*, 38(4):495–501, August 2013.

[22] S M Aldoshin, Z G Aliev, T K Goncharov, A I Kazakov, Yu M Milekhin, N A Plishkin, and N I Shishov. Structure and properties of cocrystals of trinitrotoluene and 2,4,6,8,10,12-hexanitro-2,4,6,8,10,12-hexaazaisowurtzitane. *Russian Chemical Bulletin*, 62(6):1354–1360, 2013.

[23] T K Goncharov, Z G Aliev, S M Aldoshin, D V Dashko, A A Vasileva, N I Shishov, and Yu M Milekhin. Preparation, structure, and main properties of bimolecular crystals CL-20-DNP and CL-20-DNG. *Izvestiya Akademii Nauk. Seriya Khimicheskaya*, 64(2):366–0374, 2015.

[24] ML Hobbs and MR Baer. Calibrating the bkw-eos with a large product species database and measured cj properties. In *Tenth Symposium (International) on Detonation, Boston, MA*, 1993.

[25] L. A. Kruglyakova and R. S. Stepanov. Kinetics and mechanism of the liquid phase thermolysis of 1-methyl-3,5-dinitro-1,2,4-triazole. *Russian Journal of General Chemistry*, 81(9):1918, 2011.

[26] Pasupala Ravi, Dilip M Badgujar, Girish M Gore, Surya P Tewari, and Arun K Sikder. Review on melt cast explosives. *Propellants, Explosives, Pyrotechnics*, 36(5):393–403, 2011.

[27] Stephen R. Anderson, Pascal Dubé, Mariusz Krawiec, Jerry S. Salan, David J. am Ende, and Philip Samuels. Promising CL-20-based energetic material by cocrystallization. *Propellants, Explosives, Pyrotechnics*, pages n/a–n/a, 2016.

[28] David I. A. Millar, Helen E. Maynard-Casely, David R. Allan, Adam S. Cumming, Alistair R. Lennie, Alexandra J. MacKay, Iain D. H. Oswald, Chiu C. Tang, and Colin R. Pulham. Crystal engineering of energetic materials: Co-crystals of CL-20. *CrystEngComm*, 14(10):3742–3749, apr 2012.

[29] Jonathan C. Bennion, Nilanjana Chowdhury, Jeff W. Kampf, and Adam J. Matzger. Hydrogen Peroxide Solvates of 2,4,6,8,10,12-Hexanitro-2,4,6,8,10,12-hexaazaisowurtzitane. *Angewandte Chemie*, 128(42):13312–13315, oct 2016.

[30] Jonathan C Bennion, Andrew McBain, Steven F Son, and Adam J Matzger. Design and synthesis of a series of nitrogen-rich energetic cocrystals of 5,5-dinitro-2 H,2 H-3,3-bi-1,2,4-triazole (DNBT). *Crystal Growth and Design*, 15(5):2545–2549, 2015.

[31] L L Bagal, M S Pevzner, A N Frolov, and N I Sheludyakova Khimiya. HETERO-CYCLIC NITRO COMPOUNDS I. Synthesis Of Nitro Derivatives Of. *Geterot-siklicheskikh Soedinenii*, 6(2):259–264, 1970.

[32] Alexander A. Dippold and Thomas M. Klapötke. Nitrogen-rich bis-1,2,4-triazoles - A comparative study of structural and energetic properties. *Chemistry - A European Journal*, 18(52):16742–16753, dec 2012.

[33] Ren A. Wiscons, Michael Bellas, Jonathan C. Bennion, and Adam J. Matzger. Detonation performance of ten forms of 5,5'-dinitro-2H,2H'-3,3'-bi-1,2,4-triazole (DNBT). *Crystal Growth & Design*, page acs.cgd.8b01583, nov 2018.

[34] JWAM Janssen, HJ Koeners, C Gr Kruse, and Clarisse L Habrakern. Pyrazoles. xii. preparation of 3 (5)-nitropyrazoles by thermal rearrangement of n-nitropyrazoles. *The Journal of Organic Chemistry*, 38(10):1777–1782, 1973.

[35] Robert D. Schmidt, Gregory S. Lee, Philip F. Pagoria, Alexander R. Mitchell, and Richard Gilardi. Synthesis of 4-amino-3, 5-dinitro-1H-pyrazole using vicarious nucleophilic substitution of hydrogen. *Journal of Heterocyclic Chemistry*, 38(5):1227–1230, sep 2001.

[36] Alan DeHope, Mao Xi Zhang, K Thomas Lorenz, Edward Lee, Damon Parish, and Philip F Pagoria. Synthesis and Small-scale Performance Characterization of New Insensitive Energetic Compounds. *Insensitive Munitions & Energetic Materials Technology Symposium (IMEMTS)*, (May), 2015.

[37] A W Campbell. Diameter Effect and Failure Diameter of a TATB-Based Explosive. *Propellants, Explosives, Pyrotechnics*, 9(6):183–187, 1984.

[38] David Chavez, Larry Hill, Micheal Hiskey, and Scott Kinkead. Preparation and explosive properties of azo-and azoxy-furazans. *Journal of Energetic Materials*, 18(2-3):219–236, 2000.

[39] Jonathan C. Bennion, Zohaib R. Siddiqi, and Adam J. Matzger. A melt castable energetic cocrystal. *Chem. Commun.*, 53(45):6065–6068, Jun 2017.

[40] Ren A. Wiscons and Adam J. Matzger. Evaluation of the Appropriate Use of Characterization Methods for Differentiation between Cocrystals and Physical Mixtures in the Context of Energetic Materials. *Crystal Growth & Design*, 17(2):901–906, feb 2017.

[41] Margaret C. Etter. Hydrogen bonds as design elements in organic chemistry. *The Journal of Physical Chemistry*, 95(12):4601–4610, 1991.

[42] Margaret C. Etter, Susan M. Reutzel, and Carolyn G. Choo. Self-organization of adenine and thymine in the solid state. *Journal of the American Chemical Society*, 115(10):4411–4412, may 1993.

[43] Tomislav Friščič and William Jones. Recent advances in understanding the mechanism of cocrystal formation via grinding. *Crystal Growth and Design*, 9(3):1621–1637, 2009.

[44] Resonant Acoustic Mixing, 2009.

[45] David J Am Ende, Stephen R Anderson, and Jerry S Salan. Development and scale-up of cocrystals using resonant acoustic mixing. *Organic Process Research and Development*, 18(2):331–341, 2014.

[46] Stephen R Anderson, David J am Ende, Jerry S Salan, and Philip Samuels. Preparation of an energetic-energetic cocrystal using resonant acoustic mixing. *Propellants, Explosives, Pyrotechnics*, 39(5):637–640, 2014.

[47] Stephen R Anderson, Pascal Dubé, Mariusz Krawiec, Jerry S Salan, David J am Ende, and Philip Samuels. Promising cl-20-based energetic material by cocrystallization. *Propellants, Explosives, Pyrotechnics*, 41(5):783–788, 2016.

[48] Karl S Hope, Hayleigh J Lloyd, Daniel Ward, Adam A L Michalchuk, and Colin R Pulham. Resonant acoustic mixing: Its applications to energetic materials. *New Trends in Research of Energetic Materials (NTREM)*, (April 2015):134–143, 2015.

[49] Hongwei Qiu, Rajen B Patel, Reddy S Damavarapu, and Victor Stepanov. Nanoscale 2cl-20· hmx high explosive cocrystal synthesized by bead milling. *CrystEngComm*, 17(22):4080–4083, 2015.

[50] Cesar Medina, Dominick Daurio, Karthik Nagapudi, and Fernando Alvarez-Nunez. Manufacture of pharmaceutical co-crystals using twin screw extrusion: A solvent-less and scalable process. *Journal of Pharmaceutical Sciences*, 99(4):1693–1696, apr 2010.

[51] Kevin Boksa, Andrew Otte, and Rodolfo Pinal. Matrix-assisted cocrystallization (MAC) simultaneous production and formulation of pharmaceutical cocrystals by hot-melt extrusion. *Journal of pharmaceutical sciences*, 103(9):2904–2910, sep 2014.

[52] Keqian Zhang and Dejie Li. *Electromagnetic Theory for Microwaves and Optoelectronics.* Springer, 2008.

[53] Sophocles J. Orfanidis. Electromagnetic waves and antennas.

[54] G. F. Cawsey, J. L. Farrands, and S. Thomas. Observations of Detonation in Solid Explosives by Microwave Interferometry. *Proceedings of the Royal Society A: Mathematical, Physical and Engineering Sciences*, 248(1255):499–521, December 1958.

[55] Albert D. Krall, Brian C. Glancy, and Harold W. Sandusky. Microwave interferometry of shock waves. I. Unreacting porous media. *Journal of Applied Physics*, 74(10):6322–6327, November 1993.

[56] J. W. Tringe, R. J. Kane, K. S. Vanderall, F. Garcia Converse, F. Garcia, and C. M. Tarver. Microwave Interferometry for Understanding Deflagration-to-Detonation and Shock-to-Detonation Transitions in Porous Explosives. Technical report, Lawrence Livermore National Laboratory (LLNL), Livermore, CA, 2014.

[57] Brian C. Glancy, Harold W. Sandusky, and Albert D. Krall. Microwave interferometry of shock waves. II. Reacting porous media. *Journal of Applied Physics*, 74(10):6328–6334, November 1993.

[58] Melvin A. Cook, Ray L. Doran, and Glen J. Morris. Measurement of Detonation Velocity by Doppler Effect at ThreeCentimeter Wavelength. *Journal of Applied Physics*, 26(4):426–428, apr 1955.

[59] Leon D. Strand, August L. Schultz, and Gary K. Reedy. Microwave doppler shift technique for determining solid propellant transient regression rates. *Journal of Spacecraft and Rockets*, 11(2):75–83, 1974.

[60] LEON D. STRAND, AUGUST L. SCHULTZ, and GARY K. REEDY. Microwave Doppler Shift Technique for Determining Solid Propellant Transient Regression Rates. *Journal of Spacecraft and Rockets*, 11(2):75–83, feb 1974.

[61] Gene H. McCall, Wayne L. Bongianni, and Gilbert A. Miranda. Microwave interferometer for shock wave, detonation, and material motion measurements. *Review of Scientific Instruments*, 56(8):1612–1618, 1985.

[62] BA Aničin, Branislav Jojić, Djordje Blagojević, M Adžić, and V Milosavljević. Flame plasma and the microwave determination of solid propellant regression rates. *Combustion and flame*, 64(3):309–319, 1986.

[63] Blaine W. Asay. *Shockwave Science and Technology Reference Library Volume 5-Non-Shock Initiation of Explosives*. Springer, 2010.

[64] Philip Rae, Brian Glover, Jake Gunderson, Lee Perry, Philip J Rae, Brian B Glover, Jake A Gunderson, and W Lee Perry. Free-field microwave interferometry for detonation front tracking and run-to-detonation measurements free-field microwave interferometry for detonation front tracking and run-to-detonation measurements. In *APS Shock Compression of Condensed Matter*, 2011.

[65] Gabriel G. Luther and Barry J. Warthen. Microwave interferometry to elucidate shock properties. In *AIP Conference Proceedings*, volume 309, pages 1755–1757. AIP, 1994.

[66] V M Bel 'skii, A L Mikhailov, A V Rodionov, and A A Sedov. Microwave Diagnostics of Shock-Wave and Detonation Processes. *Fizika Goreniya i Vzryva*, 47(6):639–650, 2011.

[67] Robert S. Janesheski, Lori J. Groven, and Steven F. Son. Detonation failure characterization of homemade explosives. *Propellants, Explosives, Pyrotechnics*, 39(4):609–616, 2014.

[68] David E. Kittell, Jesus O. Mares, and Steven F. Son. Using time-frequency analysis to determine time-resolved detonation velocity with microwave interferometry. *Review of Scientific Instruments*, 86(4):044705, 2015.

[69] Sorin Bastea and Laurence E. Fried. Chemical equilibrium detonation. In *Shock Wave Science and Technology Reference Library*, pages 1–31. Springer Berlin Heidelberg, Berlin, Heidelberg, 2012.

[70] Jerry W. Forbes. *Shock wave compression of condensed matter: A Primer*. Springer Berlin Heidelberg, Berlin, Heidelberg, 2012.

[71] Henry. Eyring, Richard E. Powell, George H. Duffy, and Ransom B. Parlin. The Stability of Detonation. *Chemical Reviews*, 45(1):69–181, August 1949.

[72] W. B. White, S. M. Johnson, and G. B. Dantzig. Chemical Equilibrium in Complex Mixtures. *The Journal of Chemical Physics*, 28(5):751–755, may 1958.

[73] R. D. Cowan and W. Fickett. Calculation of the detonation properties of solid explosives with the Kistiakowsky-Wilson equation of state. *The Journal of Chemical Physics*, 24(5):932–939, may 1956.

[74] M Cowperthwaite and WH Zwisler. The jcz equations of state for detonation products and their incorporation into the tiger code. In *Sixth Symposium (International) on Detonation*, volume 162, 1976.

[75] SJ Jacobs. Recent advances in condensed media detonations. *ARS Journal*, 30(2):151–158, 1960.

[76] Mortimer J Kamlet and S J Jacobs. Chemistry of detonations. I. A simple method for calculating detonation properties of C-H-N-O explosives. *The Journal of Chemical Physics*, 48(1):23–35, 1968.

[77] T.R. Gibbs, A. Popolato, and J.F. Baytos. *LASL Explosive Property Data*. Los Alamos Scientific Laboratory Serie Son Dynamic Material Properties, Vol 4. University of California Press, 1980.

[78] Stefan Ek and Nikolaj V. Latypov. Four syntheses of 4-Amino-3,5-dinitropyrazole. *Journal of Heterocyclic Chemistry*, 51(6):1621–1627, nov 2014.

[79] Vasant S Vuppuluri, Jonathan C Bennion, Ren A Wiscons, I Emre Gunduz, Adam J Matzger, and Steven F Son. Detonation velocity measurement of a hydrogen peroxide solvate of cl-20. *Propellants, Explosives, Pyrotechnics*.

[80] Rodney L Willer. Synthesis of high-nitrogen content heterocyclic nitramines and energetic internal plasticizers. Technical report, MORTON THIOKOL INC ELKTON MD ELKTON DIV, 1987.

[81] Edward Layer and Krzysztof Tomczyk. *Hilbert transform*, volume 16. Springer, Cham, 2015.

[82] Peter L. M. Heydemann. Determination and correction of quadrature fringe measurement errors in interferometers. *Applied Optics*, 20(19):3382, October 1981.

[83] Walter Gander, Gene H. Golub, and Rolf Strebel. Least-squares fitting of circles and ellipses. *BIT*, 34(4):558–578, dec 1994.

[84] Megan E. Daily, Brian B. Glover, Steven F. Son, and Lori J. Groven. X-Band Microwave Properties and Ignition Predictions of Neat Explosives. *Propellants, Explosives, Pyrotechnics*, 38(6):810–817, dec 2013.

[85] D Steinberg. Comparison of experimental data on detonation velocity and cj pressure vs he density with predictions from ree model eos. In *Proceedings of the 8th Symposium (International) on Detonation*, pages 565–575, 1985.

[86] J Kurrle. Hmx detonation vs density. *Report OSAO*, (4148):901–003.

[87] Vasant S. Vuppuluri, Philip J. Samuels, Kelley C. Caflin, I. Emre Gunduz, and Steven F. Son. Detonation Performance Characterization of a Novel CL-20 Cocrystal Using Microwave Interferometry. *Propellants, Explosives, Pyrotechnics*, 42, 2017.

[88] Donald L Ornellas, John H Carpenter, and Stuart R Gunn. Detonation calorimeter and results obtained with pentaerythritol tetranitrate (petn). *Review of Scientific Instruments*, 37(7):907–912, 1966.

[89] HY Afeefy, JF Liebman, and SE Stein. Nist chemistry webbook, nist standard reference database number 69. *Linstrom PJ, Mallard WG, editors*, 2011.

[90] Betsy M Rice, Sharmila V Pai, and Jennifer Hare. Predicting heats of formation of energetic materials using quantum mechanical calculations. *Combustion and Flame*, 118(3):445–458, 1999.

[91] Zongwei Yang, Haojing Wang, Yuan Ma, Qi Huang, Jichuan Zhang, Fude Nie, Jiaheng Zhang, and Hongzhen Li. Isomeric cocrystals of cl-20: A promising strategy for development of high-performance explosives. *Crystal Growth & Design*, 18(11):6399–6403, 2018.

[92] Robert W Molt Jr, Rodney J Bartlett, Thomas Watson Jr, and Alexandre P Bazant. Conformers of cl-20 explosive and ab initio refinement using perturbation theory: implications to detonation mechanisms. *The Journal of Physical Chemistry A*, 116(49):12129–12135, 2012.

[93] Binghui Duan, Yuanjie Shu, Ning Liu, Bozhou Wang, Xianming Lu, and Yingying Lu. Direct insight into the formation driving force, sensitivity and detonation performance of the observed cl-20-based energetic cocrystals. *CrystEngComm*, 20(38):5790–5800, 2018.

[94] Qing Ma, Tao Jiang, Yu Chi, Ya Chen, Jun Wang, Jinglun Huang, and Fude Nie. A novel multi-nitrogen 2, 4, 6, 8, 10, 12-hexanitrohexaazaisowurtzitane-based energetic co-crystal with 1-methyl-3, 4, 5-trinitropyrazole as a donor: experimental and theoretical investigations of intermolecular interactions. *New Journal of Chemistry*, 41(10):4165–4172, 2017.

[95] Mario Lefebvre. *Applied probability and statistics.* Springer Science & Business Media, 2007.

[96] Rao V Dukkipati. *Probability and statistics for scientists and engineers.* New Academic Science, 2011.

[97] Eric Jones, Travis Oliphant, Pearu Peterson, et al. SciPy: Open source scientific tools for Python, 2001–. [Online; accessed ¡today¿].

APPENDICES

A. INITIAL SHOT ANALYSIS CODE

```python
import numpy as np
import scipy as sp
import sys
import time
from math import *
import pandas as pd
import matplotlib.pyplot as mp
import analysis_fcns as af
from curvefit_fcns import *
from ellipse_fit_functions import *
import os
import scipy.fftpack as fftpack
mp.close('all')
#————————————Import raw data————————————————#
#shotID = raw_input('Please enter shot ID: ')
shotID = 'TS12–HMX'
filename = '/Users/vasant/Desktop/MI_Experiments/Raw_Data/' +
    shotID  + '.csv'
raw = pd.read_csv(filename, error_bad_lines=False, skiprows=0,
    nrows=100000,names=['A','B','C','D'], na_filter=False)
dim = raw.shape
r = dim[0]
t =[]
CH1 = []
```

```
CH2 = []
CH3 = []
#CH4 = []
t = np.zeros(r)
CH1 = np.zeros(r)
CH2 = np.zeros(r)
CH3 = np.zeros(r)
#CH4 = np.zeros(r)
for i in range(0,r):
    t[i] = raw.iloc[i,0]
    CH1[i] = raw.iloc[i,1]
    CH2[i] = raw.iloc[i,2]
    CH3[i] = raw.iloc[i,3]
#    CH4[i] = raw.iloc[i,4]
del raw, r
#for i in range(len(CH1)):
#    if CH1[i] == float('Inf'):
#        CH1[i] = 0.025+0.157
#    if CH1[i] == float('-Inf'):
#        CH1[i] = -0.025+0.157
#for i in range(len(CH2)):
#    if CH2[i] == float('Inf'):
#        CH2[i] = 0.05+0.08
#    if CH2[i] == float('-Inf'):
#        CH2[i] = -0.05+0.08
#————————————————Shot Information————————————————#
l0 = 3e8/35e9
lc = 11.12e-3
er_tmd = 3.4
```

```python
rho_tmd = 1.905
m0 = 9.6838 - 8.4599
rho0 = m0 /( pi/4*.2565**2*1.004*2.54**3)
er = ((er_tmd**(1./3)-1)*rho0/rho_tmd + 1) ** 3
l_t = l0 / sqrt(er - (l0/lc)**2);
#----------------Desample----------------------------------#
Fs1 = (t.size -1) / (t[t.size -1]-t[0])
n = t.size
Fs2 = 200e6
(tm,CH1) = np.array(desample(t,CH1,Fs2))
(tm,CH2) = np.array(desample(t,CH2,Fs2))
(tm,CH3) = np.array(desample(t,CH3,Fs2))
#(tm,CH4) = np.array(desample(t,CH4,Fs2))
t = tm
del tm
#for i in range(len(CH1)):
#    if CH1[i] == float('Inf'):
#        CH1[i] = 0.09
#    if CH1[i] == float('-Inf'):
#        CH1[i] = -0.09
#for i in range(len(CH2)):
#    if CH2[i] == float('Inf'):
#        CH2[i] = 0.09
#    if CH2[i] == float('-Inf'):
#        CH2[i] = -0.09
fig,ax = mp.subplots(nrows=1,ncols=1,sharex='none',sharey='
    none')
ax1 = ax.twinx()
ax.set_xlabel('Time_($\mu$s)')
```

```
ax.plot(t*1e6,CH3,'g')
ax1.set_xlabel('Time_($\mu$s)')
ax1.plot(t*1e6,CH1,'b',t*1e6,CH2,'r')#,t*1e6,CH3,'g')
ax.set_ylabel('Amplitude_(V)')
ax1.set_ylabel('Amplitude_(V)')
ax.grid(which='both',axis='x')
mp.legend(('CH1','CH2','Fiber_Optic'))
mp.show()
#————————————————High—pass filtering
    ————————————————————#
CH1_hpf = hpf(CH1,2,.01,Fs2,1)
CH2_hpf = hpf(CH2,2,.01,Fs2,1)
V1_test_lpf = lpf(CH1,2,.1,Fs2,1)
V2_test_lpf = lpf(CH2,2,.1,Fs2,1)
k = 2
mp.figure(k)
mp.title('In—phase_and_quadrature_channels_after_light_
    filtering')
mp.plot(t*1e6,V1_test_lpf,t*1e6,V2_test_lpf,'r')
mp.xlabel('Time_($\mu$s)')
mp.ylabel('a.u.')
k = k + 1
#————————————————Short—Time Fourier Transform
    ————————————#
# Do STFT on entire signal to find time—varying frequency
    content
freq1,t1_stft,Zxx1 = sp.signal.stft(V1_test_lpf,Fs2,window='
    hamming',nperseg=500,nfft = 2**15, noverlap=475)
```

```python
freq2, t2_stft, Zxx2 = sp.signal.stft(V2_test_lpf, Fs2, window='
    hamming', nperseg=500, nfft = 2**15, noverlap=475)
Zxx1 = np.abs(Zxx1)
Zxx2 = np.abs(Zxx2)
Zxx1 = Zxx1/np.max(Zxx1)
Zxx2 = Zxx1/np.max(Zxx2)
freq_max1 = np.zeros(Zxx1.shape[1])
freq_max2 = np.zeros(Zxx2.shape[1])
I1 = []
for i in range(len(freq_max1)):
    Imax1 = max(Zxx1[:,i])
    freq_max1[i] = freq1[find_ind(Imax1,Zxx1[:,i])]
for i in range(len(freq_max2)):
    Imax2 = max(Zxx2[:,i])
    freq_max2[i] = freq2[find_ind(Imax2,Zxx2[:,i])]
mp.figure(k)
mp.title('Short-Time_Fourier_Transform_for_CH1')
mp.pcolormesh((t1_stft+t[0])*1e6, freq1/1e6, np.abs(Zxx1))
fig = mp.plot((t1_stft+t[0])*1e6,freq_max1/1e6,'k')
mp.xlabel('Time_$\mu$s')
#mp.ylim([0,20])
mp.ylabel('Frequency_(MHz)')
mp.colorbar()
k = k + 1

mp.figure(k)
mp.pcolormesh((t2_stft+t[0])*1e6, freq2/1e6,np.abs(Zxx2))
mp.plot((t2_stft+t[0])*1e6,freq_max2/1e6,'k')
mp.xlabel('Time_$\mu$s')
```

```
mp.ylabel('Frequency_(MHz)')
#mp.ylim([0,20])
mp.colorbar()
k = k + 1
#——————————Select desired portion of data for analysis
    ————————————#
#ti = np.float(input('Please provide estimate of start time:
    '))
#tf = np.float(input('Please provide estimate of end time: ')
    )
pad = 0.1e−6
ti = 3.25e−6
ti_pad = ti − pad
tf = 7.6e−6
tf_pad = tf+pad


(ind_pad_i,ind_pad_f) = cut(ti_pad,tf_pad,t)
CH1_pad = CH1[ind_pad_i:ind_pad_f]
CH2_pad = CH2[ind_pad_i:ind_pad_f]
CH3_pad = CH3[ind_pad_i:ind_pad_f]
tpad = t[ind_pad_i:ind_pad_f]


(ind_i,ind_f) = cut(ti,tf,t)
t = t[ind_i:ind_f]
CH1 = CH1[ind_i:ind_f]
CH2 = CH2[ind_i:ind_f]
CH3 = CH3[ind_i:ind_f]
#t = t − t[0]
mp.figure(k)
```

```python
mp.plot(t*1e6,CH1,'b',t*1e6,CH2,'r')
mp.title('Signals_after_selecting_start_and_end_times')
mp.xlabel('Time_($\mu$s)')
mp.ylabel('Voltage_(V)')
mp.grid()
k = k + 1
#————————————————————FFT————————————————————#
frq1,I1,Y1 = find_fft(CH1,Fs2)
frq2,I2,Y2 = find_fft(CH1,Fs2)


mp.figure(k)
mp.title('FFT_for_Channel_1')
mp.plot(frq1/1e6,I1)
mp.xlabel('Frequency_(MHz)')
mp.ylabel('Intensity_(dB)')
mp.grid()
k = k + 1


mp.figure(k)
mp.plot(frq2/1e6,I2)
mp.title('FFT_for_Channel_2')
mp.xlabel('Frequency_(MHz)')
mp.ylabel('Intensity_(dB)')
mp.grid()
k = k + 1


del frq1,I1,Y1,frq2,I2,Y2
#————————————————Filter  Data
    ————————————————#
```

```
CH1_hpf = hpf(CH1,2,.01,Fs2,1)
CH2_hpf = hpf(CH2,2,.01,Fs2,1)
V1f = lpf(CH1_hpf,2,.09,Fs2,1)
V2f = lpf(CH2_hpf,2,.09,Fs2,1)
V1 = lpf(CH1,2,.09,Fs2,1)
V2 = lpf(CH2,2,.09,Fs2,1)


V1_norm = normalize_zc(V1)
V2_norm = normalize_zc(V2)
mp.figure(k)
mp.title('Normalized Signals')
mp.xlabel('Time ($\mu$s)')
mp.plot(t*1e6,V1,t*1e6,V2,'r')
mp.legend(['V1','V2'])
k = k + 1
#————————————————————STFT
    ————————————————————————#
freq1,t1_stft,Zxx1 = sp.signal.stft(V1f,Fs2,window='hamming',
    nperseg=300,nfft = 2**12, noverlap=299)
freq2,t2_stft,Zxx2 = sp.signal.stft(V2f,Fs2,window='hamming',
    nperseg=300,nfft = 2**12, noverlap=299)
Zxx1 = np.abs(Zxx1)
Zxx2 = np.abs(Zxx2)
Zxx1 = Zxx1/np.max(Zxx1)
Zxx2 = Zxx1/np.max(Zxx2)
freq_max1 = np.zeros(Zxx1.shape[1])
freq_max2 = np.zeros(Zxx2.shape[1])
I1 = []
for i in range(len(freq_max1)):
```

```python
    Imax1 = max(Zxx1[:,i])
    freq_max1[i] = freq1[find_ind(Imax1,Zxx1[:,i])]
for i in range(len(freq_max2)):
    Imax2 = max(Zxx2[:,i])
    freq_max2[i] = freq2[find_ind(Imax2,Zxx2[:,i])]
mp.figure(k)
mp.pcolormesh(t1_stft*1e6, freq1/1e6, np.abs(Zxx1))
mp.plot(t1_stft*1e6,freq_max1/1e6,'k')
mp.xlabel('Time_$\mu$s')
mp.ylim([0,20])
mp.ylabel('Frequency_(MHz)')
mp.title('STFT_for_Channel_1')
mp.colorbar()
k = k + 1

mp.figure(k)
mp.pcolormesh(t2_stft*1e6, freq2/1e6,np.abs(Zxx2))
mp.plot(t2_stft*1e6,freq_max2/1e6,'k')
mp.xlabel('Time_$\mu$s')
mp.ylim([0,20])
mp.ylabel('Frequency_(MHz)')
mp.title('STFT_for_Channel_2')
mp.colorbar()
k = k + 1

fmean = np.zeros(len(freq_max1))
for i in range(len(fmean)):
    fmean[i] = np.mean([freq_max1[i],freq_max2[i]])
v = l_t/2*fmean
```

```python
fs = len(t1_stft)/(t1_stft[len(t1_stft)-1]-t1_stft[0])
vf = lpf(v,2,.1,fs,1)
x = sp.integrate.cumtrapz(vf,t1_stft)*1000
t_pos = np.linspace(t1_stft[0],t1_stft[len(t1_stft)-1],len(x)
    )
mp.figure(k)
mp.title('Position_vs._time_plot_using_STFT')
mp.plot(t_pos*1e6,x,'o')
mp.ylabel('position_(mm)')
mp.xlabel('time_($\mu$s)')
mp.grid()
k = k + 1
del i
#——————————Find curve fit parameters————————
    ——————————#
(X1, Xtest1, res1) = LM(t,0,V1_norm)
#yhat1 = normalize_zc(ypred(X1,t))
yhat1 = normalize_zc(ypred(X1,t))


(X2, Xtest2, res2) = LM(t,0.05,V2_norm)
#yhat2 = normalize_zc(ypred(X2,t))
yhat2 = normalize_zc(ypred(X2,t))



Y1 = np.fft.fft(V1_norm)
frq1 = np.fft.fftfreq(len(V1_norm))*Fs2


Y2 = np.fft.fft(V2_norm)
frq2 = np.fft.fftfreq(len(V2_norm))*Fs2
```

```python
f1 = frq1[find_ind(max(np.abs(Y1)),np.abs(Y1))]
f2 = frq2[find_ind(max(np.abs(Y2)),np.abs(Y2))]


phase1 = np.zeros(len(Y1))
phase2 = np.zeros(len(Y2))
for i in range(len(phase1)):
    phase1[i] = atan2(np.imag(Y1[i]),np.real(Y1[i]))
del i
for i in range(len(phase1)):
    phase2[i] = atan2(np.imag(Y2[i]),np.real(Y2[i]))
del i


X1[3] = np.mean(phase1)
X2[3] = np.mean(phase2)
f1 = af.downsample(freq_max1,len(t))
f2 = af.downsample(freq_max2,len(t))
ypred1_test = X1[0]*exp(-X1[1]*t)*np.cos(2*pi*f1*t+np.mean(
    phase1))+X1[4]
ypred2_test = X2[0]*exp(-X2[1]*t)*np.sin(2*pi*f2*t+np.mean(
    phase2))+X2[4]
ypred1_test = normalize_zc(ypred1_test)
ypred2_test = normalize_zc(ypred2_test)
#------------Calculate perecent difference
    ------------------------#
diff1 = normalize_zc(abs(ypred1_test/V1_norm) - 1) # %
    difference for first plot
diff2 = normalize_zc(abs(ypred2_test/V2_norm) - 1) # %
    difference for second plot
```

```python
mp.figure(k)
mp.title('Curve_fit_for_Channel_1')
mp.plot(t*1e6,V1_norm,'b',t*1e6,yhat1,'r')
k = k + 1
mp.figure(k)
mp.title('Curve_fit_for_Channel_2')
mp.plot(t*1e6,V2_norm,'b',t*1e6,yhat2,'r')
k = k + 1

mp.figure(k)
mp.title('Curve_fit_for_Channel_1_with_FFT_Phase')
mp.plot(t*1e6,V1_norm,t*1e6,ypred1_test,'g')
k = k + 1
mp.figure(k)
mp.title('Curve_fit_for_Channel_2_with_FFT_Phase')
mp.plot(t*1e6,V2_norm,t*1e6,ypred2_test,'g')
k = k + 1
#————————Estimate start and end time windows
    ————————————————#
ti_start_CH1 = 4.884e-6
tf_start_CH1 = 4.98e-6

ti_end_CH1 = 8.4e-6
tf_end_CH1 = 8.96e-6

ind_ti_start_CH1 = find_ind(ti_start_CH1,t)
ind_tf_start_CH1 = find_ind(tf_start_CH1,t)
start_CH1 = diff1[ind_ti_start_CH1:ind_tf_start_CH1]
```

```
ind_ti_end_CH1 = find_ind(ti_end_CH1,t)
ind_tf_end_CH1 = find_ind(tf_end_CH1,t)
end_CH1 = diff1[ind_ti_end_CH1:ind_tf_end_CH1]


ti_start_CH2 = 4.807e-6
tf_start_CH2 = 4.91e-6


ti_end_CH2 = 8.46e-6
tf_end_CH2 = 8.74e-6


ind_ti_start_CH2 = find_ind(ti_start_CH2,t)
ind_tf_start_CH2 = find_ind(tf_start_CH2,t)
start_CH2 = diff2[ind_ti_start_CH2:ind_tf_start_CH2]


ind_ti_end_CH2 = find_ind(ti_end_CH2,t)
ind_tf_end_CH2 = find_ind(tf_end_CH2,t)
end_CH2 = diff2[ind_ti_end_CH2:ind_tf_end_CH2]


###————————————Find start and end times
    ————————————#
ti_CH1 = 0
tf_CH1 = 0
ti_CH1 = t[find_ind(0.0005,abs(start_CH1))+ind_ti_start_CH1]
tf_CH1 = t[find_ind(0.0005,abs(end_CH1))+ind_ti_end_CH1]
ti_CH2 = 0
tf_CH2 = 0
ti_CH2 = t[find_ind(0.0005,abs(start_CH2))+ind_ti_start_CH2]
tf_CH2 = t[find_ind(0.0005,abs(end_CH2))+ind_ti_end_CH2]
```

```python
print('ti_CH1 = ',ti_CH1)
print('tf_CH1 = ',tf_CH1)

print('ti_CH2 = ',ti_CH2)
print('tf_CH2 = ',tf_CH2)


data = {'t': pd.Series((t)*1e6),'V1':pd.Series(V1_norm),'V1p'
    :pd.Series(yhat1)}
DataFrame = pd.DataFrame(data,columns=['t','V1','V1p'])
datapath = '/Users/vasant/Desktop/Research/dissertation/'
name = 'curve_fit'
DataFrame.to_csv(datapath+name+'.csv', header=False,index=
    False,index_label=None)
```

B. SHOT ANALYSIS CODE

```python
# _____


# This code will be used to analyze MI shots.
# The steps are as follows:
    # 1. Import data and create four vectors (t, CH1, CH2,
        CH3); CH1 & CH2 are
    # the reference and quadrature signals and CH3 is the
        trigger.
    # 2. Desample the data down to ~200 MHz
    # 3. Find the start and end times of the detonation event
        .
    # 4. Filter the signal
    # 5. Analyze using the quadrature method.
# _____


import numpy as np
import scipy as sp
import sys
from math import *
import pandas as pd
import matplotlib.pyplot as mp
from find_ind import *
from analysis_fcns import *
```

```python
from curvefit_fcns import *
from ellipse_fit_functions import *
import os
mp.close('all')
#————————————————Import raw data————————————————#
#shotID = raw_input('Please enter shot ID: ')
shotID = 'TS1-HMX_CL20_CC'
filename = '/Users/vasant/Desktop/MI_Experiments/Raw_Data/' + \
    shotID + '.csv'
raw = pd.read_csv(filename, error_bad_lines=False, skiprows=22,
    nrows=100000, names=['A', 'B', 'C', 'D'], na_filter=False)
dim = raw.shape
r = dim[0]
t = []
CH1 = []
CH2 = []
CH3 = []
t = np.zeros(r)
CH1 = np.zeros(r)
CH2 = np.zeros(r)
CH3 = np.zeros(r)
for i in range(0, r):
    t[i] = raw.iloc[i, 0]
    CH1[i] = raw.iloc[i, 1]
    CH2[i] = raw.iloc[i, 2]
    CH3[i] = raw.iloc[i, 3]
del raw, r
#————————————————Test Sample Information
    ————————————————#
```

```
l0 = 8.56e-3
lc = 11.12e-3
er_tmd = 3.5
rho_tmd = 1.945
rho0 = 1.415
#rho0 = 1.407
er = ((er_tmd**(1./3)-1)*rho0/rho_tmd + 1) ** 3
l_t = l0 / sqrt(er - (l0/lc)**2);
#---------------------Desample---------------------------------------#
Fs1 = (t.size-1) / (t[t.size-1]-t[0])
n = t.size
Fs2 = 200e6
(tm,CH1) = np.array(desample(t,CH1,Fs2))
(tm,CH2) = np.array(desample(t,CH2,Fs2))
(tm,CH3) = np.array(desample(t,CH3,Fs2))
t = tm
del tm
#---------------Select desired portion of data for analysis
    ---------------------#
# In this section, the signal is cut to the desired length.
    Two sets of data
# result from the processes in this section-padded and
    unpadded. The Hilbert
# transform used for normalization has edge artifacts. The
    signal is padded
# by including an extra portion of the waveform data before
    and after the
# timeframe for analysis.
pad = 0.1e-6
```

```
ti = 2.5e-6
#ti = 2.373e-6
ti_pad = ti - pad
tf = 5.875e-6
#tf = 5.972e-6
tf_pad = tf+pad


(ind_pad_i , ind_pad_f) = cut(ti_pad , tf_pad , t)
CH1_pad = CH1[ind_pad_i:ind_pad_f]
CH2_pad = CH2[ind_pad_i:ind_pad_f]
tpad = t[ind_pad_i:ind_pad_f]


(ind_i , ind_f) = cut(ti , tf , t)
t = t[ind_i:ind_f]
CH1 = CH1[ind_i:ind_f]
CH2 = CH2[ind_i:ind_f]
#t = t - t[0]
#-------------------------------Filter Data
    ------------------------#
V1 = lpf(CH1,2 ,.07 ,1)
V2 = lpf(CH2,2 ,.07 ,1)
V1_pad = lpf(CH1_pad,2 ,.07 ,1)
V2_pad = lpf(CH2_pad,2 ,.07 ,1)


#------------------------Normalize using a constant parameter
    --------------------------#
# Note that the the _pad_norm and _norm datasets are the same
    . One is padded with
# and the other is unpadded.
```

```
V1_pad_norm = normalize_zc(V1_pad)
V2_pad_norm = normalize_zc(V2_pad)
V1_norm = normalize_zc(V1)
V2_norm = normalize_zc(V2)
#———————————————Normalize using envelope function
    ————————————#
H1 = sp.signal.hilbert(V1_pad_norm)
H2 = sp.signal.hilbert(V2_pad_norm)
V1n_h = V1_norm/np.abs(H1[ind_i−ind_pad_i:ind_f−ind_pad_f])
V2n_h = V2_norm/np.abs(H2[ind_i−ind_pad_i:ind_f−ind_pad_f])
#———————————————Obtain correction factors
    ———————————————#
# Data from an ideal quadrature mixer plotted as (V1,V2)
    would yield a perfect
# circle. The combination of nonorthongality of the in−phase
    and quadrature
# channels, unequal channel gain, and zero offset distorts a
    perfect circle
# to a distorted ellipse, represented as rotation, stretching
    , and translation
# of a perfect circle. The normalized (using envelope)
    signals are fit to an
# ellipse of the form [x,y] = [z1,z2] + Q(alpha)*[a*cos(t),b*
    sin(t)].
[z,a,b,alpha] = fitellipse(np.mat([V1n_h,V2n_h]),constraint='
    bookstein',tol=1e−5)
A = np.mat([[1/a,0],[0,1/b]])
Qnorm = Q(alpha)
Vtrans = np.mat([V1n_h−z[0],V2n_h−z[1]])
```

```python
# The stretching, rotation, and translation of a perfect
    circle is represented as
# [V1,V2] = [a,0,0,b]*Q*[V1p,V2p] + [zx,zy] (p denotes
    perfect signal)
Vcorr = np.matmul(A,np.matmul(np.transpose(Qnorm),Vtrans))
V1c = np.array(Vcorr[0,:]).flatten()
V2c = np.array(Vcorr[1,:]).flatten()


V1c = normalize_zc(V1c)
V2c = normalize_zc(V2c)
#——————————Create phase and velocity plots
    ————————————#
# This is with normalization with a constant parameter
phi = np.zeros(len(CH1))
L = 1.004*25.4
for i in range(len(phi)):
    phi[i] = atan2(V2_norm[i],V1_norm[i])
phi = phase_unwrap(phi)
l_tdyn = 4*pi*L/(phi[len(phi)-1]-phi[0])
x = np.zeros(len(phi))
xdyn = np.zeros(len(phi))
for i in range(len(x)):
    x[i] = l_t*1000 / (4*pi) * phi[i]
    xdyn[i] = l_tdyn / (4*pi) * phi[i]
x = x - x[0]
xdyn = xdyn - xdyn[0]
t = t - t[0]
```

```python
s = sp.stats.linregress(t*1e6,x)
sdyn = sp.stats.linregress(t*1e6,xdyn)
mp.plot(t*1e6,x)
U = s.slope
Udyn = sdyn.slope
Uest = L/((tf-ti)*1e6)


print('Wavelength using measured permittivity: ',l_t*1000, '
    mm.')
print('Dynamically determined wavelength: ',l_tdyn , ' mm.')


print('Estimated detonation velocity is: ',Uest, ' km/s ,')
print('Detonation velocity using measured wavelength is: ',U,
     ' km/s.')
print('Detonation velocity using dynamic wavelength is: ',
    Udyn, ' km/s.')


#-----------------------Create phase and velocity plots
    ------------------

# This is with the Hilbert normalization
phi_h = np.zeros(len(V1c))
L = 1.004*25.4
for i in range(len(phi_h)):
    phi_h[i] = atan2(V2c[i],V1c[i])
phi_h = phase_unwrap(phi_h)
lh_tdyn = 4*pi*L/(phi_h[len(phi_h)-1]-phi_h[0])
lh_t = l_t
xh = np.zeros(len(phi_h))
xh_dyn = np.zeros(len(phi_h))
```

```
for i in range(len(xh)):
    xh[i] = lh_t*1000 / (4*pi) * phi_h[i]
    xh_dyn[i] = lh_tdyn / (4*pi) * phi_h[i]
xh = xh - xh[0]
xh_dyn = xh_dyn - xh_dyn[0]
t = t - t[0]


sh = sp.stats.linregress(t*1e6,xh)
shdyn = sp.stats.linregress(t*1e6,xh_dyn)
mp.plot(t*1e6,xh)
Uh = sh.slope
Uh_dyn = shdyn.slope


print('Wavelength using measured permittivity (Hilbert): ',
    lh_t*1000, ' mm.')
print('Dynamically determined wavelength (Hilbert): ',lh_tdyn
    , ' mm.')


print('Detonation velocity using measured wavelength and 
    Hilbert normalization is: ',Uh, ' km/s.')
print('Detonation velocity using dynamic wavelength and 
    Hilbert normalization is: ',Uh_dyn, ' km/s.')


#——————Write x-t plots to csv file
    ————————————————#
#data = {'t': pd.Series(t*1e6),'x':pd.Series(xh)}
#DataFrame = pd.DataFrame(data,columns=['t','x'])
#datapath = '/Users/vasant/Desktop/Research/HMX_CL20 Paper/
    Position-Time Data/'
```

```
#DataFrame.to_csv(datapath+shotID+'_position_time'+'.csv',
    header=False,index=False,index_label=None)


pad = 0.1e-6
ti = 0e-6
ti_pad = ti - pad
tf = 13e-6
tf_pad = tf+pad


(ind_pad_i,ind_pad_f) = cut(ti_pad,tf_pad,t)
CH1_pad = CH1[ind_pad_i:ind_pad_f]
CH2_pad = CH2[ind_pad_i:ind_pad_f]
tpad = t[ind_pad_i:ind_pad_f]


(ind_i,ind_f) = cut(ti,tf,t)
t = t[ind_i:ind_f]
CH1 = CH1[ind_i:ind_f]
CH2 = CH2[ind_i:ind_f]
CH3 = CH3[ind_i:ind_f]


data = {'t': pd.Series((t-t[0])*1e6),'V1':pd.Series(V1c),'V2'
    :pd.Series(V2c)}
DataFrame = pd.DataFrame(data,columns=['t','V1','V2'])
datapath = '/Users/vasant/Desktop/Research/dissertation/'
name = 'normalized_hilbert'
DataFrame.to_csv(datapath+name+'.csv', header=False,index=
    False,index_label=None)
```

VITA

VITA

Vasant Swarup Vuppuluri was born August 12, 1988 in Portland, OR. He earned his Bachelor of Science in Mechanical Engineering from University of Portland in 2010. He earned his Master of Science in Mechanical Engineering from Portland State University in July 2015. He entered Purdue in the Fall of 2015 and finished his PhD in the Spring of 2019.